SSCL-Preprint-159

SSCL-Preprint-159
October 1992
Distribution Category: 414

J. Siegrist

# Experimental Challenges at Future Hadron Colliders (Lectures for the 1992 St. Croix Summer School)

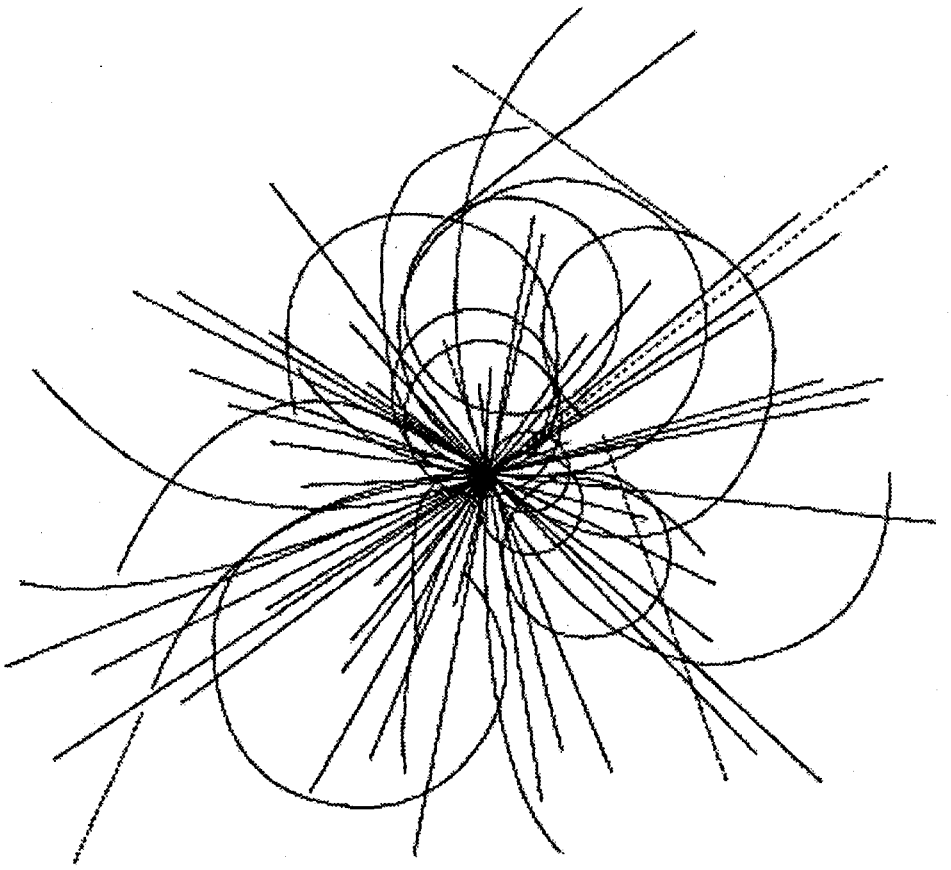

Superconducting Super Collider Laboratory

# EXPERIMENTAL CHALLENGES AT FUTURE HADRON COLLIDERS

**(Lectures for the 1992 St. Croix Summer School)**

James Siegrist

Superconducting Super Collider Laboratory *
2550 Beckleymeade Avenue
Dallas, Texas 75237

## ABSTRACT

An overview of the experimental program at future hadron colliding beam machines is presented. Special emphasis is given to the Tevatron upgrade program and Superconducting Super Collider physics with the detector designed by the Solenoidal Detector Collaboration (SDC). Expected physics reach of the new machines is outlined. Expected physics performance of the proposed SDC design is detailed.

## INTRODUCTION

### The Standard Model

The standard model has the leptons ($e\mu\tau\nu$) and quarks ($udcsbt$) as its "fundamental" particles. Electroweak and strong interactions among these fundamental particles are mediated by the gluons (strong) and the $\gamma, Z^0$, and $W^{\pm}$ (electroweak). The standard model also features an electroweak symmetry-breaking (Higgs) sector and several parameters such as the quark and lepton masses and interaction coupling strengths. Theoretical extensions of and alternatives to the standard model reduce to the standard model at low ($\ll M_W$) energy, since all experimental results are "fit" by the standard model.

However, many residual problems and questions about the standard model framework are unresolved. These include confirmation of the top quark existence, the detailed nature of electroweak symmetry breaking, the pattern of masses and mixing of the fundamental particles, the origin of CP violation, the reason for the existence of

* Operated by the Universities Research Association, Inc., for the U.S. Department of Energy under Contract No. DE-AC35-89ER40486.

generations of quarks and leptons, whether the forces are unified at a more fundamental level, the origin of the gauge symmetries, *etc.* Many of these questions will be directly or indirectly addressed by the physics programs proposed for the future hadron colliders.

## The Standard Model at Hadron-Hadron Colliders

The total hadron-hadron cross section is large, ranging from around 65 mb at the Fermi National Accelerator Laboratory (FNAL) Tevatron at $\sqrt{s} = 1.8$ TeV to of order 100 mb expected for the proposed Superconducting Super Collider (SSC) experiments at $\sqrt{s} = 40$ TeV. The soft collision processes that produce many low-energy particles and give rise to most of the total cross section (so-called "$\ln(s)$" physics) will not be discussed here. These lectures concentrate on the hard-scattering processes among proton constituents that lead to events containing few, energetic products. The $\ln(s)$ physics generates a background of soft particles from which the hard constituent collisions must be separated. Since collision rates for the proton constituents can be more or less reliably estimated, hard collisions in these machines provide a laboratory for looking for new phenomena and testing standard model predictions at high $Q^2$.

For colliding beam machines, the total event rate $R$ is given by $R = \mathcal{L} \cdot \sigma_{\text{TOT}}$, where $\mathcal{L}$ is the machine luminosity and $\sigma_{\text{TOT}}$ is the total hadron-hadron cross section. For the Tevatron, luminosities achieved so far are in the range $\sim 10^{30}$ cm$^{-2}$sec$^{-1}$. For the SSC, luminosities are expected to be in range $\sim 10^{33}$ cm$^{-2}$sec$^{-1}$. For a total cross section of 60 mb, this luminosity yields a total event rate of 60 kHz at FNAL and 60 MHz for the SSC. The event size for a typical collider experiment, such as the Collider Detector at FNAL (CDF), is of order 80 kbytes of data. Electronic data acquisition systems cannot yet be constructed with the capacity to record all this information. Even if the data could be recorded, computational resources and storage capacity to fully analyze the resulting event sample do not exist.

The inability to record all events at hadron-hadron colliders is not a fatal flaw in such experiments because the interesting hard-scattering processes occur at a much lower rate. Hadron-hadron experiments require a "filter" to reduce the number of events and information per event to be recorded. For the multipurpose high $p_t$ collider experiments, filter decisions are made based on a search for final states containing the fundamental entities in the standard model. This filtering process begins in the design of the detection hardware, through the online "trigger" system, and on into the offline data analyses.

## Standard Model Tests in Hadron-Hadron Colliders

The procedure for testing the standard model by means of the event sample selected on the basis that each event contains one or more of the fundamental standard model objects begins with checks on the understanding of the detector performance for simple standard model processes, such as high $p_t$ jet production, high $p_t$ lepton production from $W$, $Z$ decay, direct photon production, *etc.* Once a reasonable understanding of the detector performance has been achieved, tests for simple standard model extensions (quark compositeness, $Z + X$ production, *etc.*) can be made based on limits on deviations from the predicted behavior. Once detailed understanding of standard model predictions has been achieved, limits on new phenomena can be set by studying the details of event configurations, searching for exclusive final states, and placing limits on standard model forbidden final states.

The ability of multipurpose detectors to find and measure such events is built in at a fundamental level. The ability to measure the "energy flow" from the quark or gluon fragmentation to hadrons is achieved via calorimetric techniques. The ability to identify final states containing electrons and muons allows searches for "odd" combinations of particles (*e.g.*, $e\mu$ events). Final states containing neutrinos are detected by the imbalance in the transverse energy flow. The result is a powerful apparatus that is able to fully visualize events and carry out many different types of standard model tests simultaneously. This results in an interlocking network of tests, all within one apparatus. The multipurpose detectors are therefore necessarily complex and expensive, and they require a large collaboration to fully exploit their physics potential.

## Future Machines and Their Physics Goals

In the past, the bulk of what we know about particle physics has been found by direct production of the particles in high-$p_t$ experiments at high-energy accelerators. This fact explains why high-$p_t$ experiments have first priority in the world HEP program. Over the coming decade, the two highest-energy machines in the U.S. will be the FNAL Tevatron and the SSC; in Europe, the Large Hadron Collider (LHC) is planned. Physics goals for the Tevatron upgrade program and for the SSC are detailed below. The LHC program is similar to that of the SSC, as discussed in the next section in more detail.

The upgrades planned for the 1990s for the Tevatron[1] are centered around the construction of a new Main Injector that will allow integrated luminosities of order 500 $\text{pb}^{-1}$ per year to be delivered to the experiments (CDF, D0) from proton-antiproton collisions at 2-TeV center-of-mass energy. The instantaneous luminosity will be in the range 0.5–1 $\times 10^{32}$ $\text{cm}^{-2}\text{sec}^{-1}$, with the time between bunch crossings in the 132–396 nsec range. The new main injector will allow $\bar{p}$ accumulation rates up to 20 mA/hour. In addition, 120-GeV extracted beam will be available while running the Tevatron in collider mode. The CDF experiment will be upgraded with new electronics and triggering hardware to handle the higher luminosity, expanded muon coverage, and secondary vertex information from the new silicon vertex detector. The D0 experiment will also upgrade the electronics for the higher luminosity and will upgrade the tracker to withstand the increased radiation levels. These experiments will provide direct experience in the high-rate, high-$p_t$ environment relevant to the SSC/LHC. The main physics goals of the Tevatron upgrade program are to find the top quark and measure its mass, and to precisely ($\delta \sim 50$ MeV) measure the mass of the $W$ boson. The combination of the top quark and $W$ boson mass measurements severely constrains the standard model, as we shall see later. The Tevatron with CDF and D0 will provide the means to directly search for new physics at the highest possible mass scales until the construction of the SSC/LHC is completed at the end of the decade.

The SSC is scheduled for completion near the end of 1999. The machine[2] will deliver $10^4$ $\text{pb}^{-1}$ per year integrated luminosity from $pp$ collisions at 40-TeV center-of-mass energy. The instantaneous luminosity will be $10^{33}$ $\text{cm}^{-2}\text{sec}^{-1}$, with 16 nsec between bunch crossings. Two complementary high-$p_t$ detectors are planned at turn-on, along with several smaller experiments. The Solenoidal Detector Collaboration[3] (SDC) design emphasizes charged particle tracking, hermetic calorimetry, good lepton identification and measurement, robust vertex detection capability, and redundancy in the particle measurements. The Gamma, Electrons, and Muons (GEM) design[4] features identification and precise measurement of photons, electrons, and muons. The design has inherent capability to operate at luminosities higher than the SSC

design. With completion this summer of the SSC magnet string test,[5] all major technical hurdles to construction of the machine have been passed.

The foremost physics goal of the SSC is to fully explore the electroweak symmetry-breaking mechanism that generates particle masses. Detailed studies of top quark production and decay will be possible at SSC. The search horizon for new phenomena such as new heavy gauge bosons, quark and lepton substructure, and supersymmetric particles will be vastly expanded by the SSC. Most of the current problem areas with the standard model will be directly or indirectly addressed by the SSC. The central issue of electroweak symmetry breaking stands out as the most important feature of the SSC experimental program.

## Physics vs. Luminosity Picture

Figures 1–7 illustrate the physics capabilities of the SSC/LHC.[6] The number of events produced by various low-background processes is plotted as a function of $\sqrt{s}$ and luminosity. Detector efficiencies and acceptances are ignored here in order to qualitatively gauge the physics reach provided by these machines.

Figure 1 shows the luminosity required to produce 20 events from a high-mass Higgs decaying to two $Z^0$, and each $Z^0$ subsequently decaying to charged leptons ($e$ or $\mu$), for various Higgs masses. In this mode, the SSC at 40 TeV and $10^{33}$ luminosity reaches beyond the 800-GeV Higgs range, while the LHC at $10^{34}$ luminosity and 10 TeV reaches just short of 800 GeV.

Figure 2 shows a similar plot for production of the intermediate-mass Higgs decaying to $ZZ^*$ with subsequent $Z$ decay to $e$ or $\mu$ for 40 events produced. The machines reach down to the 120-GeV range in this mode. No interesting limits are set on these processes at the Tevatron, as the expected production cross sections are too small.

Figure 3 shows as a function of $\sqrt{s}$ the mass for which 50 heavy quark pairs are produced per running year for various integrated luminosities. Even relatively massive heavy flavor pairs are copiously produced at the SSC and LHC. The current upper limit on the top quark mass[7] is $M_{\text{top}} > 91$ GeV from the CDF experiment at the Tevatron.

Figure 4 shows the luminosity required to produce 100 $Z'$ bosons with standard model couplings. The current CDF limit[8] is $M'_Z > 412$ GeV at 95% C.L. The SSC/LHC will greatly expand the search range, to more than 8 TeV for SSC and $\sim 4$ TeV for LHC.

Figure 5 shows the luminosity required to establish limits on various scales of quark compositeness. The current CDF limit[9] is $\Lambda_c > 1.4$ TeV at 95% C.L. The SSC should extend the limit to $\sim 20$ TeV, and the LHC to $\sim 10$ TeV.

Figure 6 shows the luminosity required to produce $10^4$ gluino pairs/year. The gluino mass limit[10] is $\geq 200$ GeV from CDF. The SSC/LHC should extend the limit to $\sim 1.5$ TeV.

Figure 7 summarizes[11] a number of SSC physics processes as a function of mass. Note that from a physics point of view, the Tevatron high-$p_t$ program feeds smoothly into the SSC program—many of the physics topics being pursued today at FNAL will continue to be pursued at SSC with much greater risk of discovery. Important additional topics encompassing electroweak symmetry breaking become accessible at the SSC for integrated luminosities above $10^{39}$ cm$^{-2}$. The current round of FNAL high-$p_t$ experiments provides direct experience in the high-rate, high-$p_t$ environment relevant to the SSC.

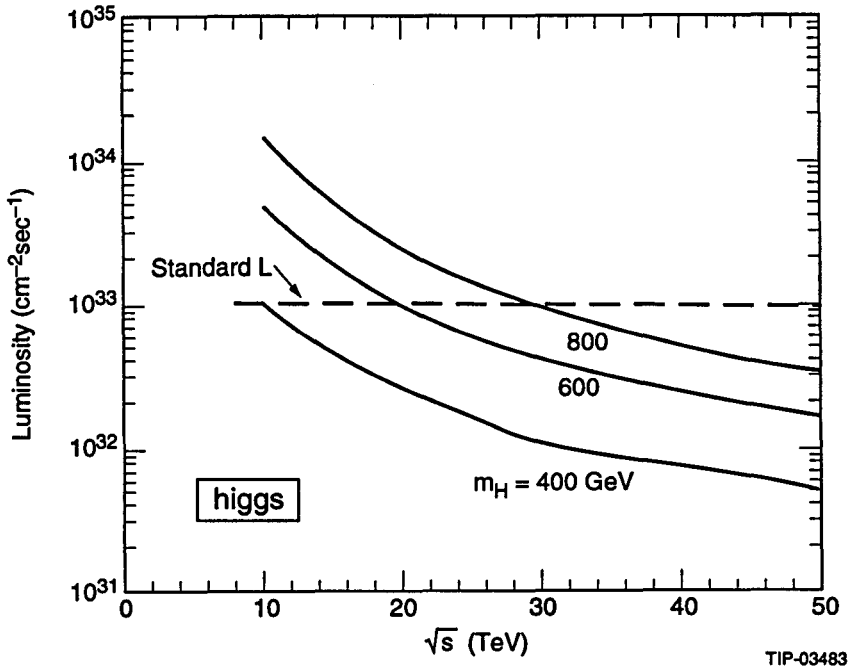


**Figure 1.** Luminosity required to produce in one year 20 Standard-Model Higgs bosons that decay to four charged leptons $(e, \mu)$ as a function of c.m. energy. (mass of $t$ quark = 85 GeV.) Results are shown for Higgs masses of 400, 600 and 800 GeV.

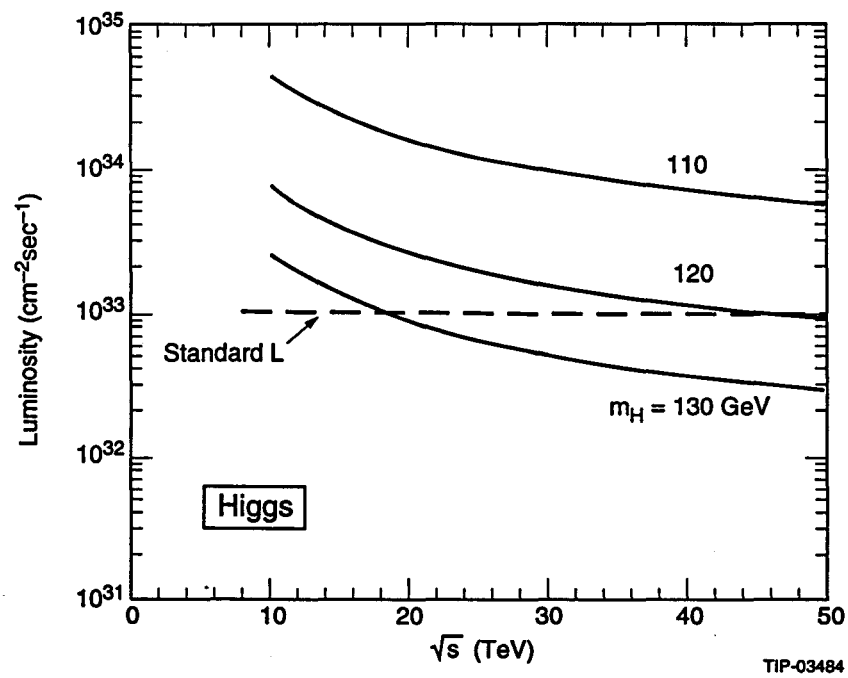


**Figure 2.** Luminosity required to produce in one year 40 intermediate mass Higgs bosons that decay into four charged leptons $(e, \mu)$ as a function of c.m. energy. (Mass of $t$ quark = 85 GeV.) Results are shown for Higgs masses of 110, 120 and 130 GeV.

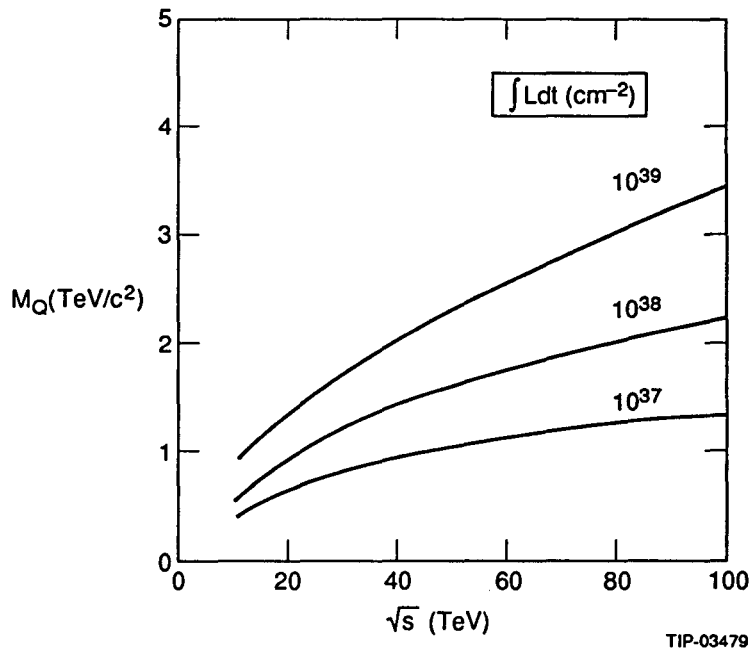


**Figure 3.** As a function of integrated luminosity, quark mass $M_Q$ reached for 50 produced $Q\bar{Q}$ pairs.

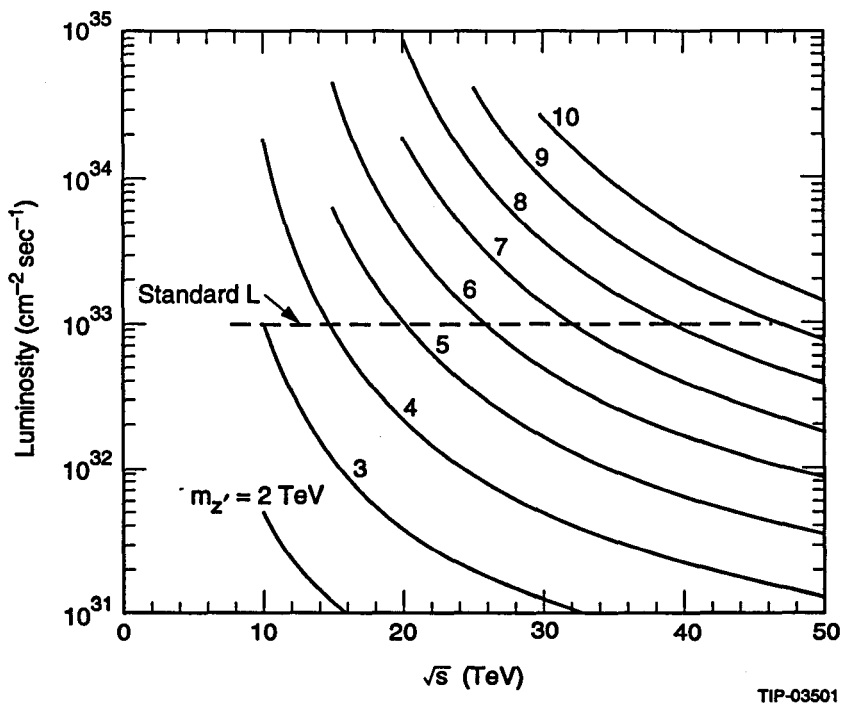


**Figure 4.** Luminosity required to produce in one year 100 $Z'$ bosons, with Standard Model couplings, as a function of c.m. energy. Results are shown for $Z'$ masses in the range from 2 to 10 TeV.

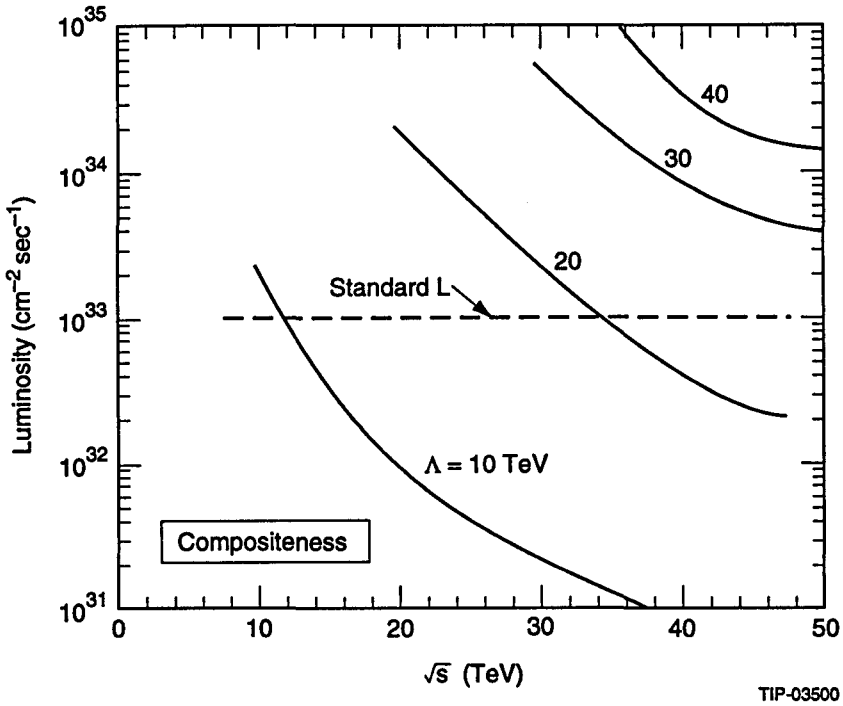


**Figure 5.** Luminosity required to establish in one year quark compositeness scales of 10, 20, 30, and 40 TeV as a function of c.m. energy.

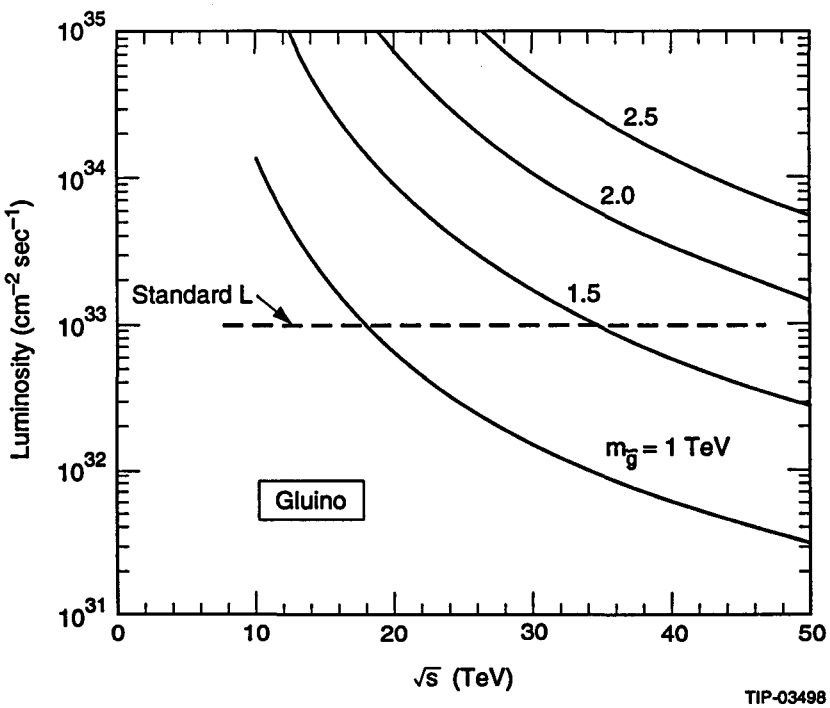


**Figure 6.** Luminosity required to produce 10 000 pairs of gluinos per year as a function of c.m. energy. Results are shown for gluino masses in the range of 1.0 to 2.5 TeV.

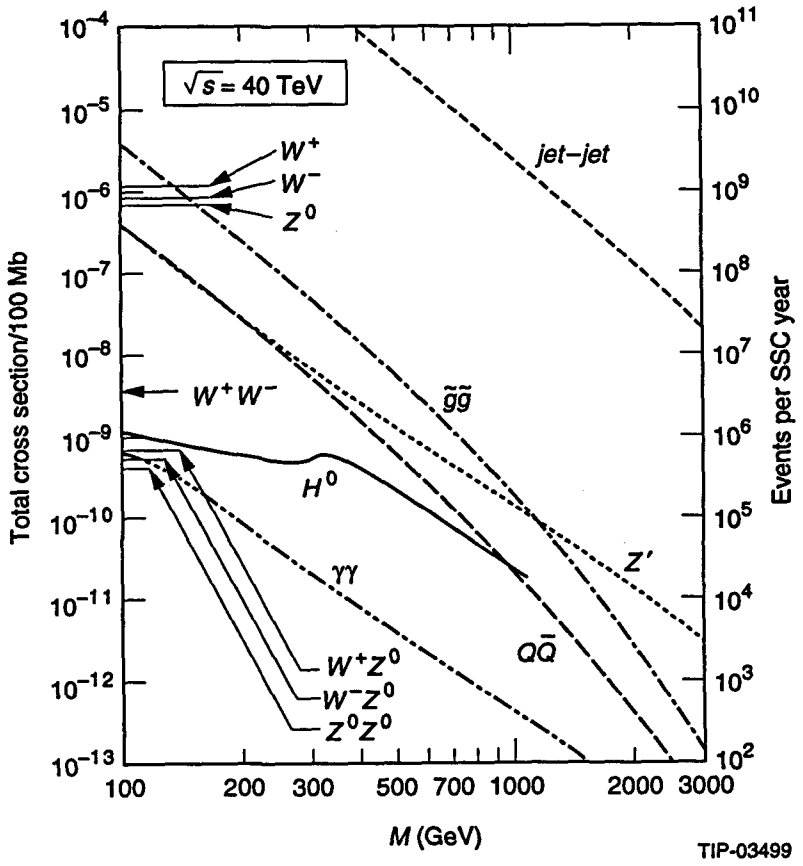


**Figure 7.** Examples of total cross sections at the SSC. The *jet-jet* and $\gamma$-$\gamma$ cross sections are for wide-angle jet or $\gamma$ pairs ($|\eta_{\rm jet}|$ and $|\eta_\gamma| < 2.5$) with invariant mass greater than $M$. For heavy-quark pair (gluino pair) production, the cross section is evaluated at $M = M_Q$ ($M = M_{\tilde{g}}$). The Higgs cross section assumes $M_{\rm top} = 150$ GeV. The left scale is total cross section divided by 100 mb, the approximate total $pp$ cross section, and so the numbers are approximate production probabilities per collision. The scale on the right is the number of produced events per year under "standard conditions," defined as operation at $\mathcal{L} = 10^{33}$ cm$^{-2}$s$^{-1}$ for $10^7$ s. These rates must be further downrated by branching fractions and experimental cuts to obtain measurable rates.

## Detector Parameterizations

In order to make the qualitative features illustrated by Figures 1–7 more quantitative, realistic detector performance must be folded into the physics capability assessment. To guide the detector design, the physics processes that demand the highest detector performance must be isolated. Certain physics processes (such as those mentioned in the previous section) can serve as qualitative guides to the general detector capabilities required. To parameterize the detector response, simple models of the SDC detector have been used. This section introduces the SDC design and the response models for the detector that are used to estimate physics performance capabilities in the following sections.

## SDC Design[11]

Figure 8 shows a perspective view of the proposed SDC design. Particles emanating from the beam collision point near the center of the detector pass in turn through the beam pipe, a silicon-strip tracker, an "outer" tracker of straw-tube design, the solenoid coil, the highly segmented electromagnetic (Em) and hadronic (HAD) calorimeters, the muon detectors, and the iron toroids of the muon detection system. Figure 9 shows a detailed view of a quarter-section of the detector.

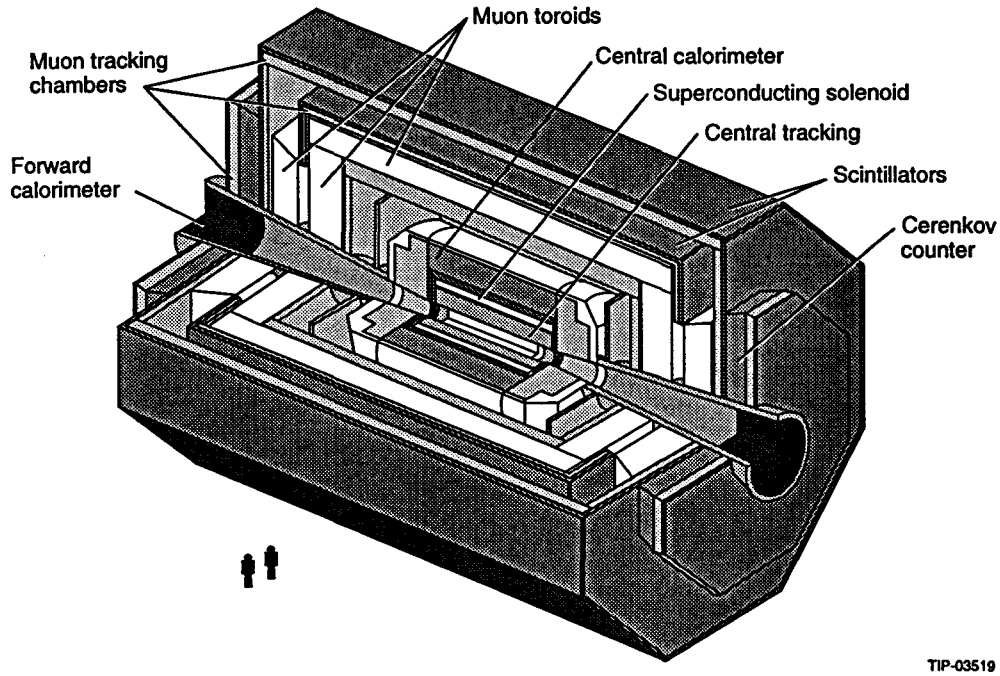


**Figure 8.** Isometric view of the preliminary baseline SDC detector configuration.

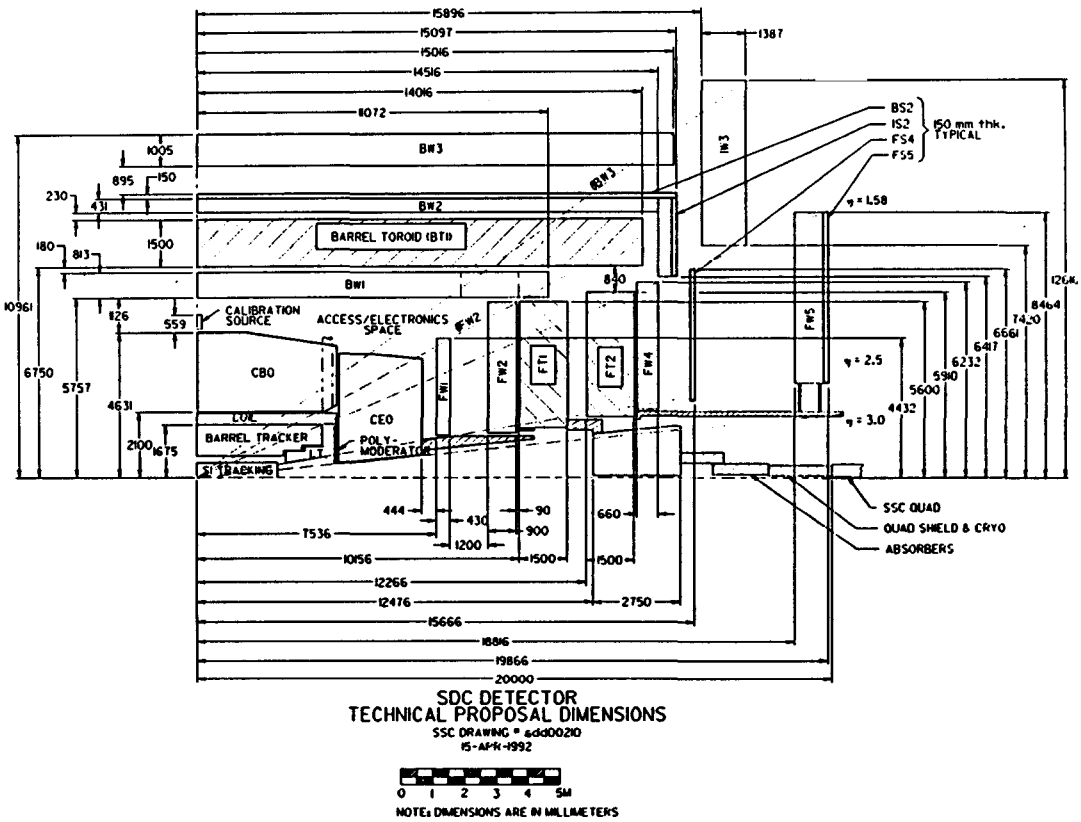


**Figure 9.** One quarter section view of the SDC design.

The model for the charged particle tracker uses a parameterized resolution that includes the effects of multiple scattering, detector resolution, and detector misalignment. When necessary, results of detailed GEANT simulations are employed, including generation of secondaries in the tracking volume. The parameterized track resolution is plotted against pseudorapidity $\eta$ in Figure 10.

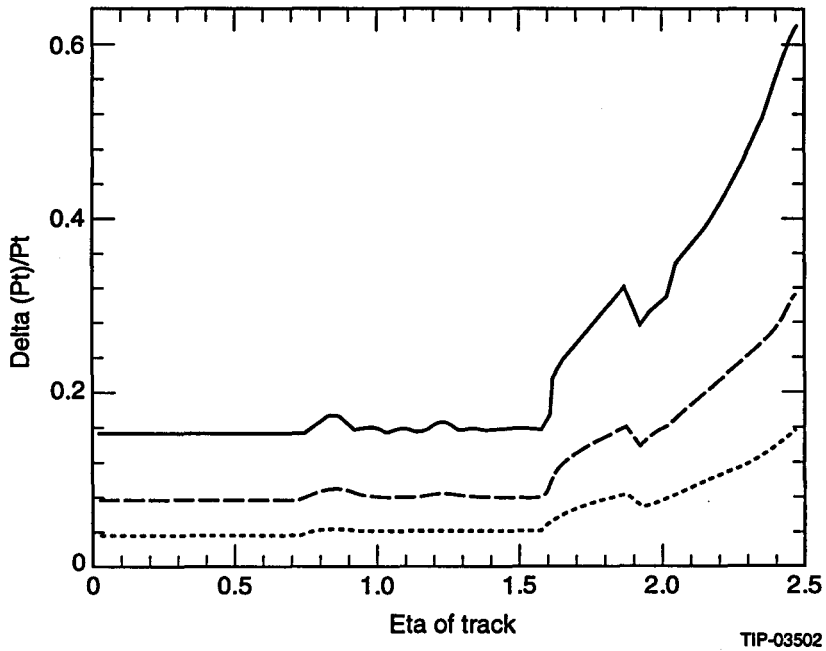


**Figure 10.** The resolution of the baseline tracking system as a function of $\eta$ for several $p_t$ values. The solid curve is for $p_t = 1000$ GeV, and the dashed (dotted) is for $p_t = 250$ (100) GeV.

Resolutions for the calorimeters are parameterized for single particles from EGS studies (Em) and CALOR89 studies (HAD) to be of the form

$$\frac{\sigma(E)}{E} = \frac{a}{\sqrt{E_t}} \oplus b \quad \text{(barrel)}$$

or

$$\frac{\sigma(E)}{E} = \frac{a}{\sqrt{E_l}} \oplus b \quad \text{(endcap)},$$

where the parameters $a$, $b$ are given in Table 1, and $\oplus$ denotes that the terms are to be added in quadrature. The hadron nonlinearity is accounted for by a $\pi/e$ response parameterized to fit CALOR89 studies with the form

$$\pi/e = \alpha - \beta/E^{0.15},$$

with the parameters $\alpha$, $\beta$ shown in Table 1. Shower shapes were parameterized from EGS (Em) and ZEUS data (HAD).

The tracking resolution parameterized for the muon system is shown in Figure 11. The parameterization includes the effects of multiple scattering in both the calorimeter and iron toroid, detector resolution, and alignment effects for the combined inner tracker and outer muon detection system.

A global efficiency of 85% for analyses requiring an isolated lepton or photon (including trigger efficiency and all selection criteria) was assumed. Results from current experiments (CDF) are used to estimate the expected background rejections against dominant backgrounds. For $p_t \gtrsim 20$ GeV, this rejection is of order $10^{-5}$ against the two-jet background.

Jets are reconstructed by using the transverse energy deposition in calorimeter cells. Seed towers with $E_t > 5$ GeV are used to define the initial jet axis. All

cells above a threshold of 100 MeV inside a cone in $\eta$-$\phi$ space are collected into the jet. Studies with ISAJET, using the single-particle calorimeter response parameters mentioned previously, lead to a jet energy resolution of

$$\frac{\sigma(E)}{E} = \frac{0.61}{\sqrt{E}} \oplus 0.016.$$

Table 1. Calorimeter Parameters.

| Parameter | Barrel | Endcap | Forward |
|---|---|---|---|
| Coverage | $\lvert\eta\rvert < 1.4$ | $1.4 < \lvert\eta\rvert < 3.0$ | $3.0 < \lvert\eta\rvert < 6.0$ |
| Radius of front face (m) | 2.10 | | |
| $z$ position of front face (m) | | 4.47 | 12.00 |
| Compartment depth | | | |
| EM (+ Coil) | 1.1 | 0.9 | |
| HAD1 | 4.1 | 5.1 | 13.0 |
| HAD2 | 4.9 | 6.0 | |
| EM resolution | | | |
| $a$ | 0.14 | 0.17 | 0.50 |
| $b$ | 0.01 | 0.01 | 0.05 |
| HAD resolution | | | |
| $a$ | 0.67 | 0.73 | 1.00 |
| $b$ | 0.06 | 0.08 | 0.10 |
| HAD nonlinearity | | | |
| $\alpha$ | 1.13 | 1.16 | 1.16 |
| $\beta$ | 0.31 | 0.38 | 0.38 |

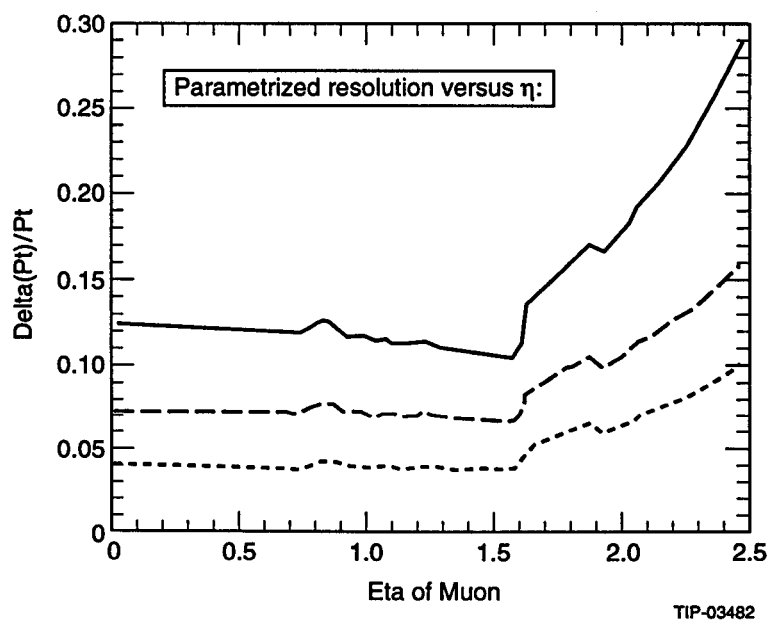


**Figure 11.** The resolution of the combined baseline tracking and muon system as a function of $\eta$ for several $p_t$ values. The solid curve is for $p_t = 1000$ GeV, and the dashed (dotted) curves are for $p_t = 250$ (100) GeV.

## STANDARD MODEL PHYSICS AT HADRON COLLIDERS[12]

The bulk of the hard-scattering cross section arises from strong interactions among the proton constituents and is accurately predicted by QCD. To illustrate the nature of the calculations, Figure 12 shows a schematic diagram of the collisions among $pp$ constituents. The partons are distributed within the proton with some distribution of fractional momentum characterized by the structure function $f$. The incoming parton interaction is described by the elementary scattering cross section $\hat{\sigma}$, and the outgoing parton lines materialize into the observed hadrons according to some fragmentation function $D$. In the final state, the two high-$p_t$ partons fragment into hadrons having limited transverse momentum with respect to the directions of the scattered partons (jets). The total $p_t$ of the dijet system is limited, and the two jets are produced back-to-back in azimuthal angle $\phi$ (see Figure 13).

In QCD, the inclusive jet yield is obtained by a folding integral over the parton distributions, each contribution being weighted by the relevant parton-parton differential cross section

$$E\frac{d^3\sigma}{d^3p} = \sum_{ij} \int dx_1 dx_2 f_i(x_1, Q^2) f_j(x_2, Q^2) \delta(\hat{s} + \hat{t} + \hat{u}) \frac{\hat{s}}{\pi} \sum_k \frac{d\sigma(ij \to k)}{d\hat{t}},$$

where $i$, $j$, $k$ sum over parton species. The differential cross section can be written in terms of the matrix element $M$ as

$$\frac{d\sigma}{d\hat{t}} = \pi \alpha_s^2(Q^2) \frac{|M|^2}{\hat{s}^2}.$$

The matrix element $|M|^2$ can be calculated in QCD, and the structure functions, along with their scaling violations, can be measured and parameterized in deep inelastic lepton-nucleon scattering. Figure 14 shows a comparison of a calculation with recent CDF data on jet production. Figure 15 shows the coordinate system for this problem. The momentum transverse to the beam direction is $p_t = p \sin\theta$. The variable $\hat{s}$, $\hat{t}$, $\hat{u}$ are given by:

$$\begin{aligned}
\hat{s} &= (p_1^\mu + p_2^\mu)^2 = x_1 x_2 s = \frac{1}{2} x_t s (x_1 \tan\theta/2 + x_2 \cot\theta/2) \\
\hat{t} &= (p_1^\mu - p^\mu)^2 = -\frac{1}{2} x_t s x_1 \tan\theta/2 = -\frac{\hat{s}}{2}(1 - \cos\theta^*) \\
\hat{u} &= (p_2^\mu - p^\mu)^2 = -\frac{1}{2} x_t s x_2 \cot\theta/2 = -\frac{\hat{s}}{2}(1 + \cos\theta^*),
\end{aligned}$$

where the initial parton $p_t = 0$, all masses are zero, $x_1 = 2p_1/\sqrt{s}$ and $x_2 = 2p_2/\sqrt{s}$ are the initial parton momentum fractions, and $x_t = 2p_t/\sqrt{s}$ is the scaled transverse momentum of the outgoing parton. Figure 15 shows the definition of $\theta^*$, the parton-parton center-of-mass scattering angle; the lab system has been boosted by an amount $P_L = \frac{\sqrt{s}}{2}(x_1 - x_2)$ along the beam axis.

Other useful variables are the rapidity $y$ defined by

$$y = \frac{1}{2} \ln\left(\frac{E + P_L}{E - P_L}\right),$$

with $E$ and $P_L$ the energy and longitudinal momentum of, *e.g.*, the parton-parton system. The pseudorapidity is defined by[13]

$$\eta = \frac{1}{2} \ln\left(\frac{P + P_L}{P - P_L}\right) = -\ln\tan\frac{\theta}{2}.$$

A change of variable and integration over azimuthal angle yields

$$E\frac{d^3\sigma}{d^3p} = \frac{1}{2\pi p_t} \frac{d^2\sigma}{dp_t d\eta}.$$

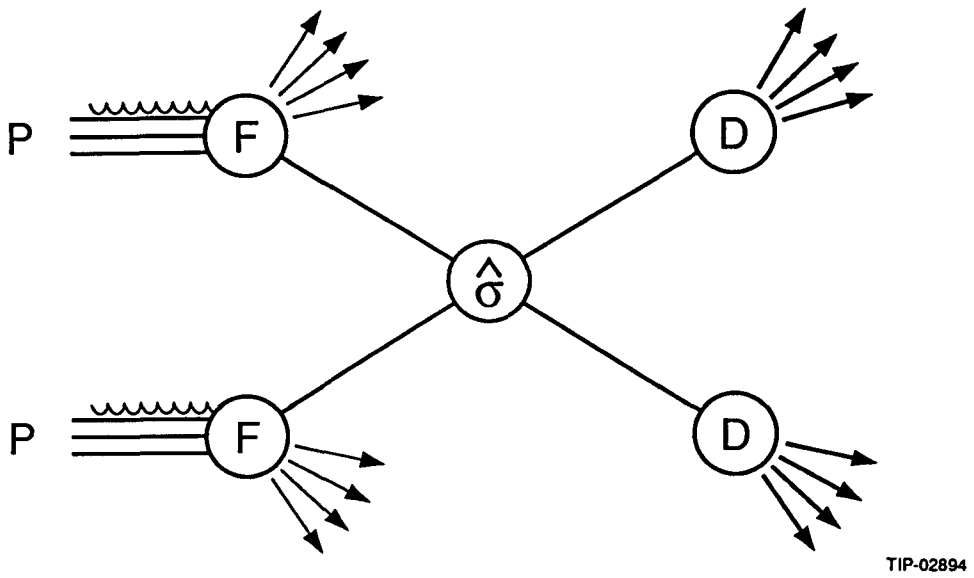


**Figure 12.** Schematic illustration of $pp$ collisions. $F$ represents the proton structure function, $\hat{\sigma}$ the elementary parton-parton scattering cross section, and $D$ the fragmentation function on the outgoing parton line.

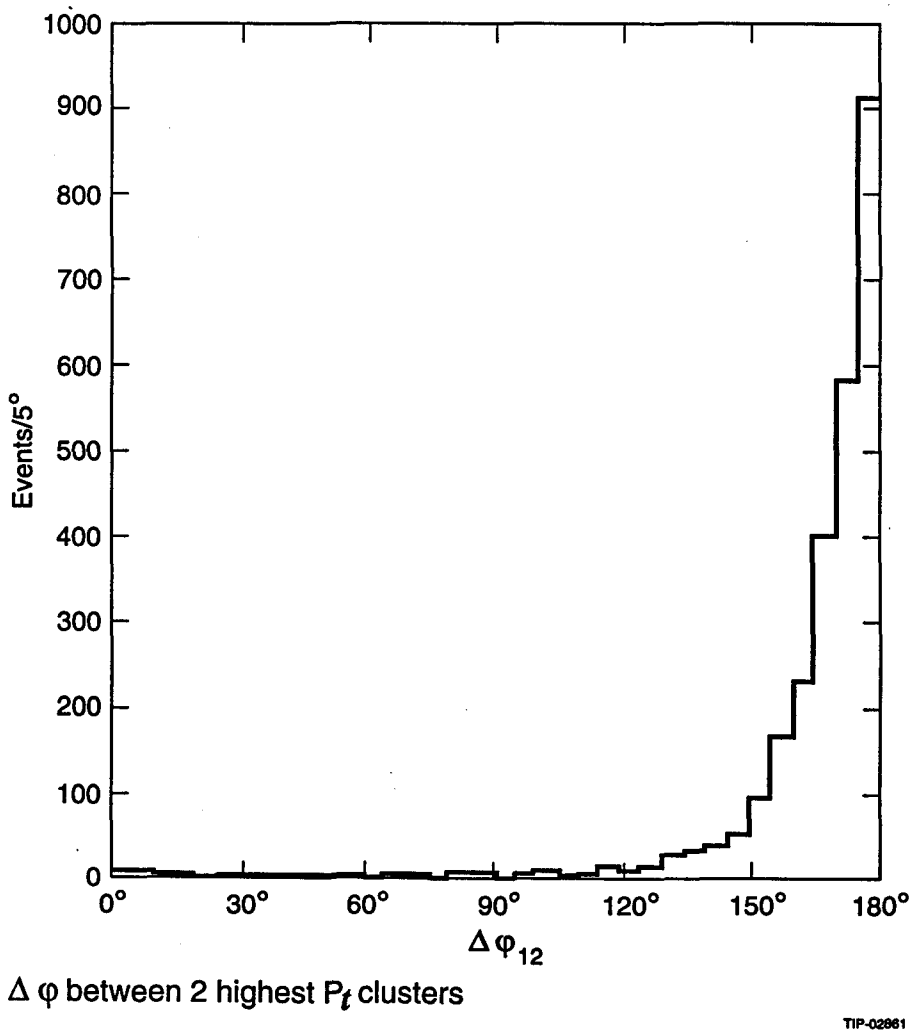


**Figure 13.** The distribution of difference in azimuth between the two clusters of highest transverse energy in a sample of events containing summed transverse energy > 60 GeV from the UA2 experiment.

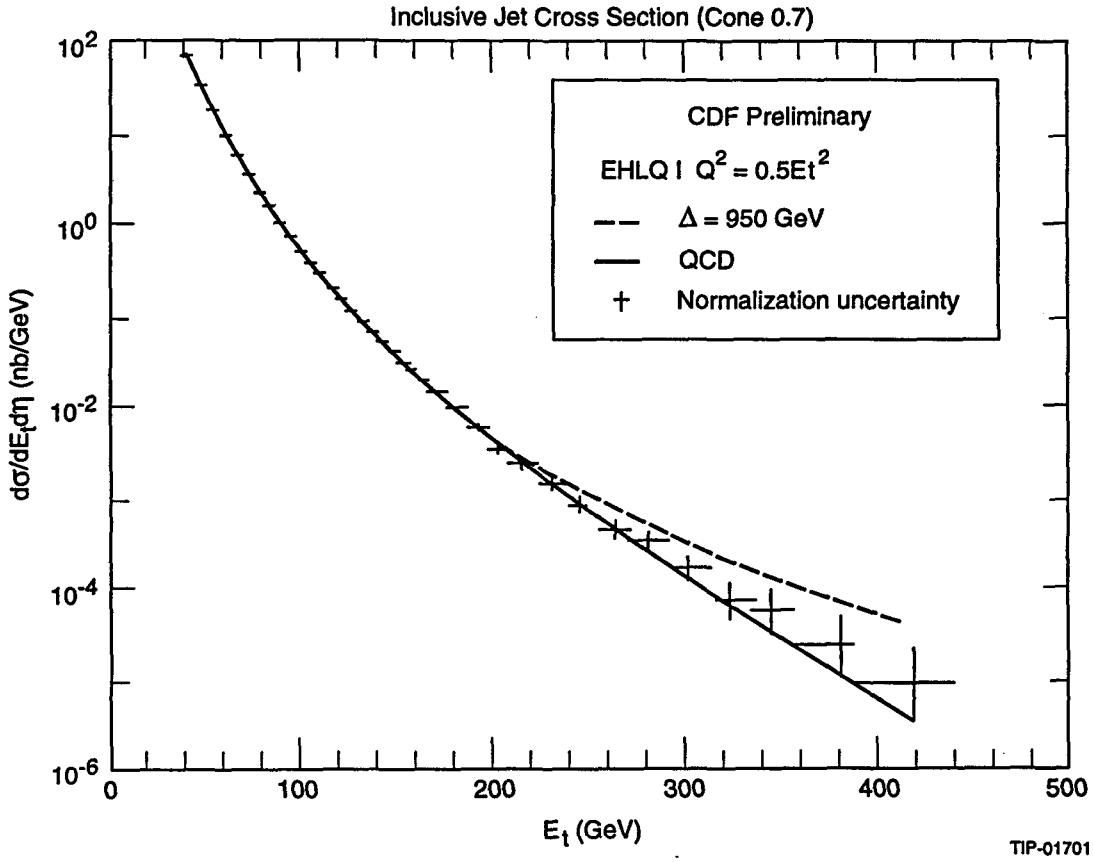


**Figure 14.** Transverse energy distribution for jets measured by the CDF collaboration.

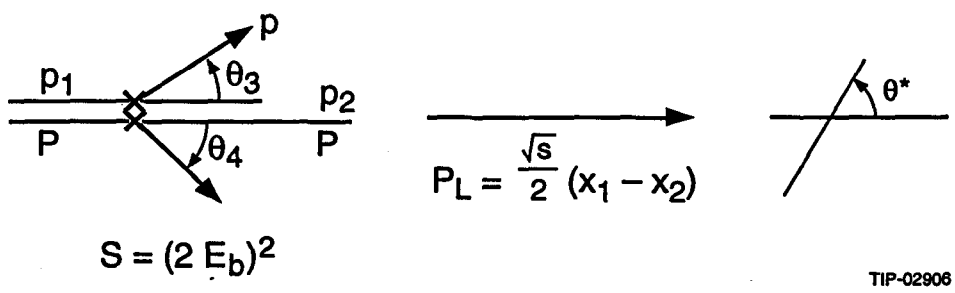


**Figure 15.** Coordinate system to describe collisions. The $z$ axis lies along the incoming proton beam. $P_1$, $P_2$ are the incoming partons, $\theta_3$ and $\theta_4$ are the outgoing scattering angles. The boost by the longitudinal momentum $P_L$ transforms to the center-of-mass system, showing the center-of-mass scattering angle $\theta^*$.

Figure 16 shows a schematic illustration of electroweak production via proton constituents of a $W$ boson, with subsequent decay to $e\nu$. This process can be calculated in the standard model in a manner completely analogous to the jet production cross section discussed earlier. In the standard model, $u+\bar{d}$ quarks couple to the $W^+$, $d+\bar{u}$ to $W^-$, and quark-antiquark pairs $u\bar{u}$, $d\bar{d}$, to the $Z^0$. The branching ratio of the $W$ to $e\nu$ final states is about 8%. The characteristic of events resulting from $W$ production is the presence of high-$p_t$ leptons ($e$, $\mu$, $\tau$) in the final state, accompanied by large missing $p_t$ from the (unmeasured) neutrinos.

Heavy flavor (top) quark pair production is also calculated in an analogous fashion. In order to set limits on top quark production, semileptonic decay modes are used to reduce background from standard model processes.

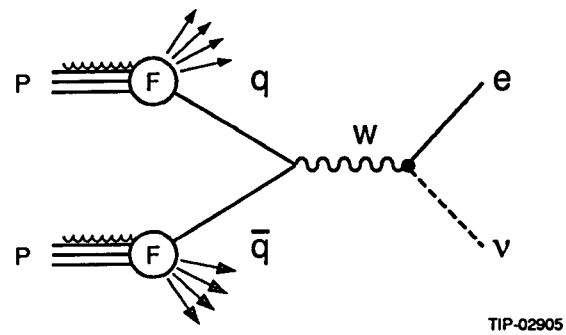


**Figure 16.** Schematic illustration of $W$ production in $pp$ collisions. $F$ represents the proton structure function; subsequent decay of the $W$ to an $e\nu$ final state is shown.

## Standard Model Measurements with the Fermilab Main Injector Upgrade[1]

The principal focus of the main injector upgrade for the Tevatron is the accurate measurement of the $W$ mass and the top quark mass. The $W$ mass is measured by forming the "transverse" mass from the lepton transverse momentum and the missing transverse momentum from the unseen neutrino. The current uncertainty on the $W$ mass is $\sim$ 350 MeV/c$^2$, limited by statistics. This uncertainty is expected to be improved to about 50 MeV after the main injector is completed. The ultimate precision that can be achieved is limited by knowledge of the proton structure function at that point. Figure 17 shows the size of the errors expected in the main injector era in $M_W$ vs. $M_{\text{top}}$. The curves are standard model predictions for various Higgs masses. These precision measurements of $M_W$, $M_{\text{top}}$ will extend our knowledge of the standard model parameters.

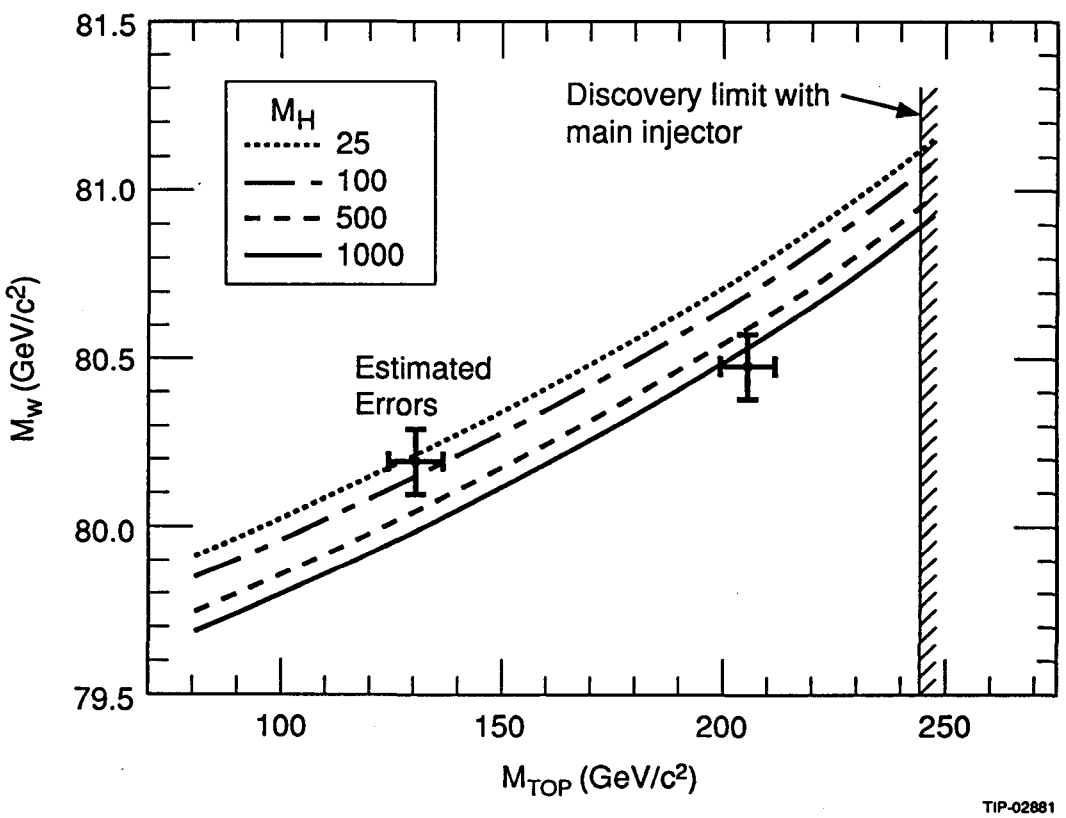


**Figure 17.** Expected precision on $M_W$ and $M_t$ with 1 pb$^{-1}$ of data collected at the Tevatron collider. Also shown are the discovery reach on $M_t$ and Standard Model predictions for various Higgs masses.

## Standard Model Physics at SSC (SDC)[11]

Several of the predictions for important SSC physics are affected by theoretical uncertainty (structure functions, behavior of initial-state radiation, higher-order corrections underlying event effects, *etc.*). The initial lower-luminosity running period of SSC will offer a unique opportunity to determine some of the unknowns involved in the theoretical calculations and to understand critical components of the detector in a rather clean environment. Typical measurements will cover inclusive and multi-jet rates and fragmentation properties, heavy quark production cross sections and properties, electroweak boson production, and multiple production of gauge bosons. Since the top quark is the most obvious system that would benefit from high-statistics studies possible at SSC, the SDC has checked the capability of the detector design for this system rather extensively. The next section details the results of some of those studies.

## Top Quark Physics at SSC

The top quark is one of the most important missing pieces in the standard model. While it may be discovered at the Tevatron before SSC begins operations, the production cross section (Figure 18) at the SSC is huge. The top will provide a window into physics beyond the standard model via its decays (*e.g.*, $t \to H^+ b$). The top is also a source of Higgs bosons via the associated production mode $pp \to t\bar{t}H$. The top is an important background to rare and exotic phenomena such as $WW$ scattering.

The main identification tools to be used in SDC to identify top are semileptonic decays and $b$-tagging. Studies have been made using the SDC detector performance described previously. Three techniques for top detection will be discussed below. The first is isolated di-leptons, *e.g.*,

$$t\bar{t} \to (t \to e\nu b) + (\bar{t} \to \mu\nu\bar{b}) .$$

The second is isolated lepton and non-isolated muon, *e.g.*,

$$t\bar{t} \to (t \to X) + (\bar{t} \to l\,\nu_l\,\mu\nu_\mu\bar{c}) .$$

The third technique is to employ lepton plus jets events, *e.g.*,

$$t\bar{t} \to (t \to e\nu b) + (\bar{t} \to jets) .$$

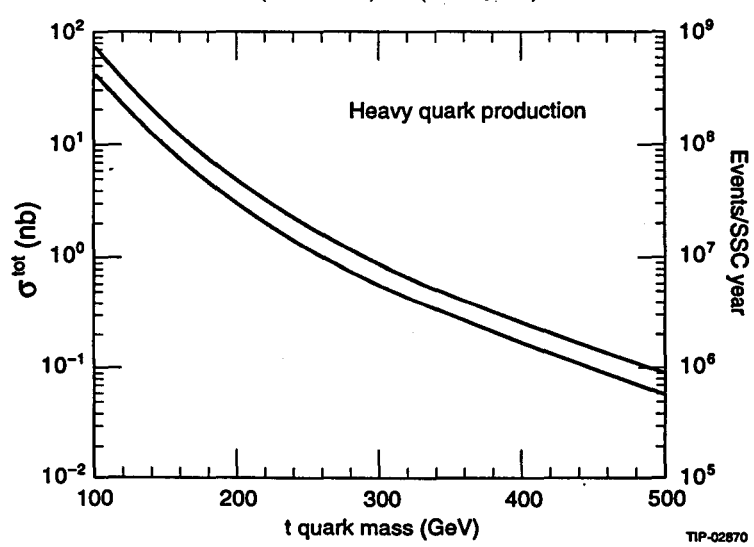


**Figure 18.** The production cross section for heavy $t$ quarks. The band corresponds to the envelope of the smallest and largest rates obtained by varying the factorization scale between 0.5 and 2 times the quark mass, and by using the following sets of structure functions: DFLM160, DFLM360, HMRSB, and MTB.

## Isolated Di-leptons

In the isolated di-lepton search, a pair of isolated $e$ and $\mu$, with $p_t > 20$ GeV and $|\eta| < 2.5$ are required. This sample is found to be background-free at the percent level, yielding $10^6$ events per SSC year ($= 10^{40}$ cm$^{-2}$) for $m_t = 150$ GeV. A comparison of the measured and predicted cross sections yields a top quark mass measurement with a mass error in the 10–15 GeV range. After subtraction of the $Z$ and Drell-Yan background, comparison of the $e\mu$ rate with the lepton pair rate can establish $e/\mu$ universality in the top decays. The $e\mu$ sample provides a clean sample of tagged $b$ jets on which to develop $b$-tagging algorithms and to verify their performance.

## Isolated Lepton and Non-Isolated Muon

Comparison of the rate for this process with the $e\mu$ rate measures the $t \to Wb$ branching ratio. This decay mode provides a better measurement of $m_t$. The selection cuts require that the electron have $p_t > 40$ GeV, with less than 4 GeV within an isolation cone of $\Delta R = 0.2$. The muon is required to have $p_t > 20$ GeV, with $> 20$ GeV within an isolation cone of $\Delta R = 0.4$. The $p_t$ of the $e\mu$ system is required to be above 100 GeV, and the azimuthal angle between the $e$ and $\mu$ must be less than 80°, to reduce opposite-charm background. The fit to the $e\mu$ mass distribution is shown in Figure 19. The left curve is for $m_t = 150$ GeV; the right is for $m_t = 180$ GeV. To check consistency, the results for different $p_t(e\mu)$ cuts ($> 60$, 100, 140 GeV) are shown in Figure 20. Using this technique, statistical errors are found to be 0.5 GeV ($m_t = 150$ GeV) or 0.8 GeV ($m_t = 250$ GeV), and backgrounds are small. Systematic errors on the $t$ mass arise from the $b$ quark fragmentation uncertainties, and the top quark $p_t$ distribution uncertainties (Figure 21). The final result is that the top quark mass uncertainty for 150 GeV mass is $\pm 0.5$ GeV (statistical) and $\pm 2.4$ GeV (systematic); for 250 GeV mass, $\pm 0.8$ GeV (statistical) and $\pm 3.9$ GeV (systematic). These results are a factor 3–4 more accurate than for the $e$-$\mu$ cross section comparison.

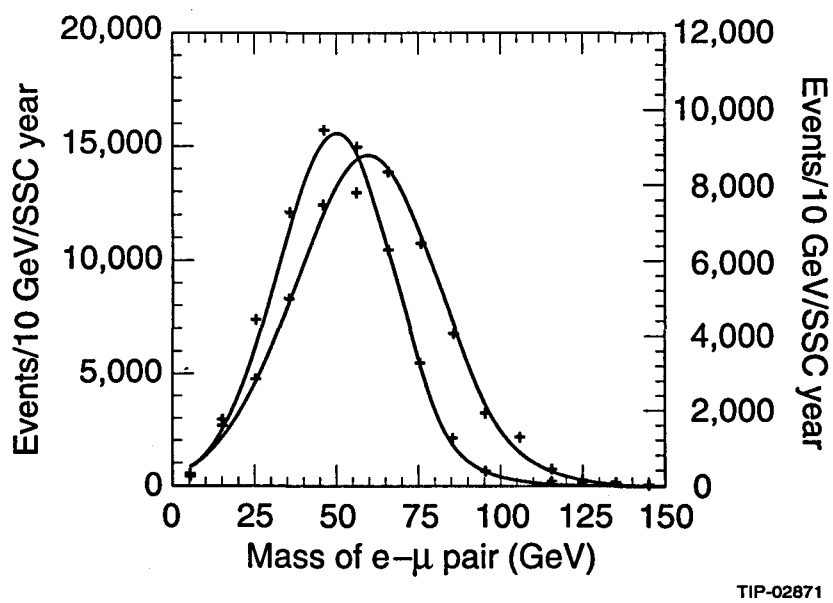


**Figure 19.** The invariant mass distribution for the $e\mu$ pair, $M(e\mu)$, for two different $t$-Quark masses. The lefthand scale and the leftmost curve are for $M_{\text{top}} = 150$ GeV, while the righthand scale and curve are for $M_{\text{top}} = 180$ GeV. The cut $p_t(e\mu) > 100$ GeV has been used. The superimposed curves represent Gaussian fits.

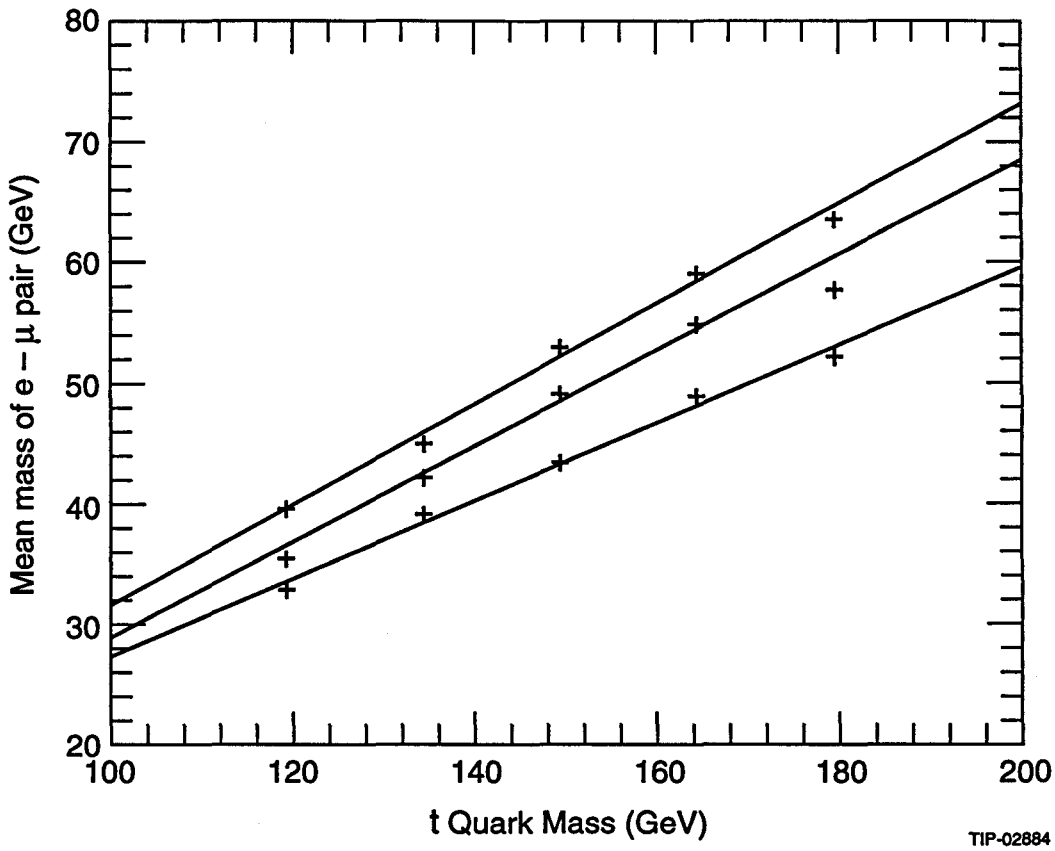


**Figure 20.** The mean invariant mass of the $e\mu$ pair as a function of the $t$-quark mass for $p_t(e\mu) >$ 60 GeV (lower curve), $p_t(e\mu) > 100$ GeV, and $p_t(e\mu) > 140$ GeV (upper curve). The data are derived from Gaussian fits to distributions such as those shown in Figure 19.

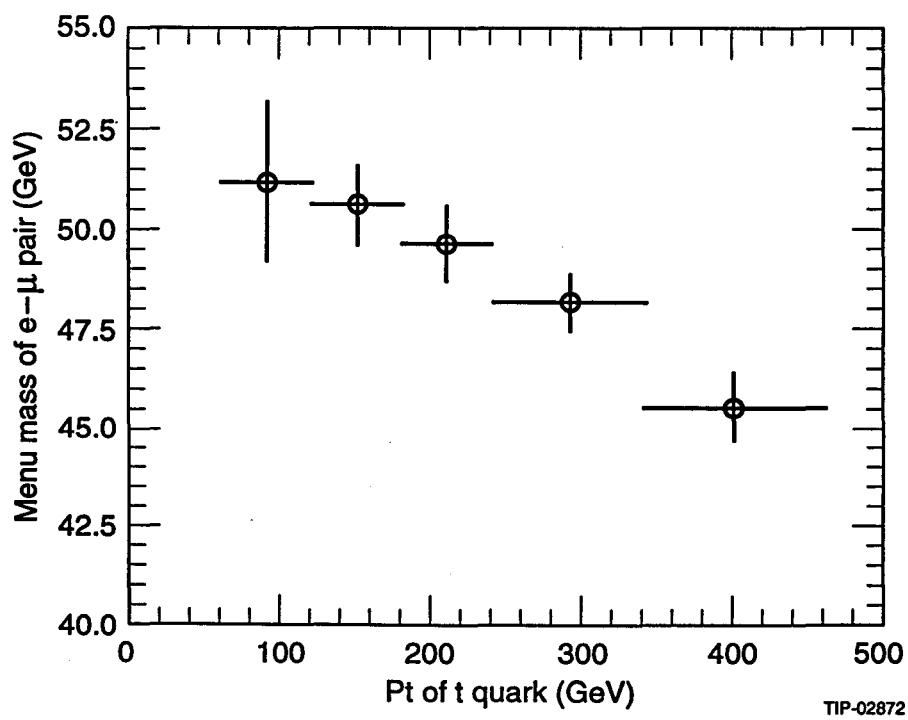


**Figure 21.** The invariant mass of the $e\mu$ pair as a function of the $t$-quark $p_t$ for $p_t(e\mu) > 100$ GeV. The data are derived from Gaussian fits to distributions such as those shown in Figure 19, for different $t$-quark $p_t$ bins.

## Lepton and Jets

In the lepton and jets mode, the invariant mass of the $t \to 3$ jets system can be measured, using the large $p_t$ of the top to reduce combinatorial background. For this analysis, jets in the region $|\eta| < 2.5$ are found using a cone size of 0.4. Leptons are required to have $|\eta| < 2.5$ and $p_t > 40$ GeV, with isolation cuts in a cone of radius 0.4 about the lepton. Energy corrections are applied to each individual jet to account for the calorimeter response discussed previously and for out-of-cone energy losses. The $t \to 3$ jets decay mode is searched for by requiring $\geq 3$ jets with $p_t > 30$ GeV and $\Delta\phi$ from each jet to the lepton $> 90°$. A $b$ tag (3 or more tracks $> 3\sigma$ from the primary vertex) is required among the jets, and the $p_t$ of the 3-jet system is required to be $> 200$ (300) GeV for $m_t = 150$ (250) GeV. Figure 22 shows the 3-jet invariant mass for events where a pair of jets has a mass within 15 GeV of the $W$ mass. Figure 23 shows the 2-jet mass distribution for events with 3-jet masses within 15 GeV of the top mass. If the 2-jet mass distribution is fixed to the $W$ mass, the resulting 3-jet systematic mass error on the top mass is estimated to be $\sim 3$ GeV.

These studies show that detection and study of the top quark at SSC will allow detailed determination of its properties. After a look at standard model extensions and physics beyond the standard model, we will return to the issue of electroweak symmetry breaking.

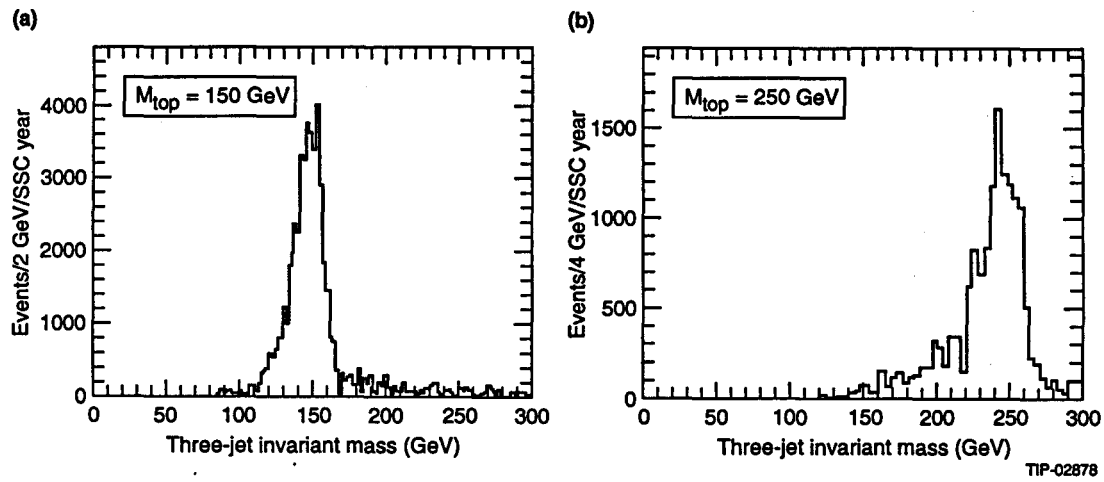


**Figure 22.** The corrected three-jet invariant mass distribution, for (a) $M_{\text{top}} = 150$ GeV and (b) $M_{\text{top}} = 250$ GeV. In this plot the two-jet invariant mass is required to be consistent with the $W$ mass $65 < M(2\text{-}jet) < 95$ GeV.

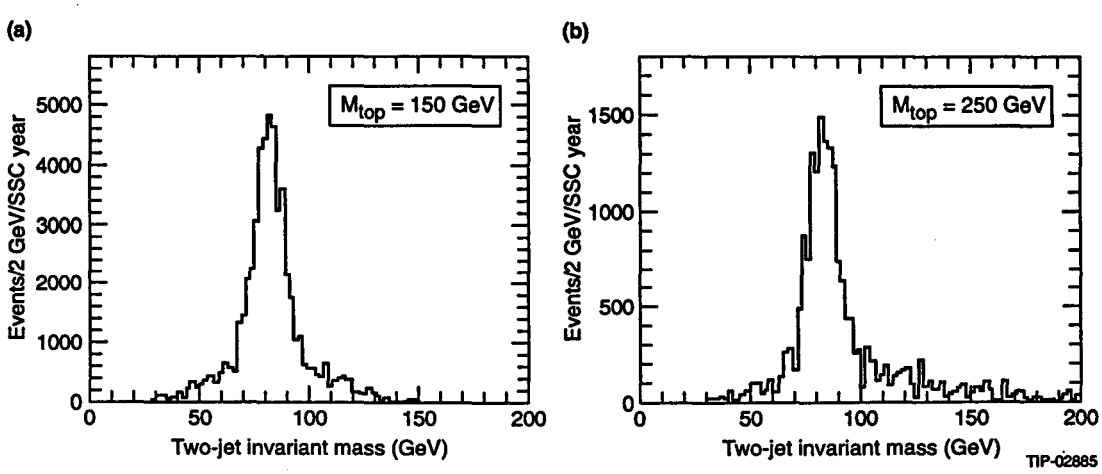


**Figure 23.** The corrected two-jet invariant mass distributions after requiring that the three-jet invariant mass be consistent with the $t$ mass. (a) $M_{\text{top}} = 150$ GeV, requiring $135 < M(3\text{-}jet) < 165$ GeV. (b) $M_{\text{top}} = 250$ GeV, requiring $225 < M(3\text{-}jet) < 275$ GeV.

## STANDARD MODEL EXTENSIONS

The FNAL Main Injector will extend searches for new physics in several areas. Quark or lepton substructure up to mass scales of order 3 TeV, supersymmetric particles (gluinos) up to 250-GeV mass, $Z'$ bosons up to 750-GeV mass, and surprises in $W^+W^-$ production can be seen after the Main Injector upgrade. To look in more detail at SDC capability for searching for simple extensions to the standard model, new heavier gauge bosons, $W'$ and $Z'$, have been considered. For new $W'$, discovery up to 5 TeV should be straightforward, since there are $\sim 10$ events for typical L-R symmetric models for this mass. For the $Z'$ case, a class of $Z'$ which arises in $E_6$ models[14] with one free parameter $\cos\alpha$ has been considered. To untangle the properties of these $Z'$s, the mass and width, production cross section, and angular distributions need to be measured. The production cross section measurement determines couplings, but it depends upon assumptions about branching ratios to exotic channels. The angular distributions directly measure the couplings, with the forward/backward asymmetry being a particularly powerful measurement. Table 2 summarizes the predictions on properties of various $E_6$-inspired $Z'$, a $Z'$ with standard $Z^0$ couplings, and $\cos\alpha = -0.6$, a value that makes the forward-backward asymmetry particularly large. Figures 24 and 25 show the mass distributions for a perfect detector (dotted), $Z' \to ee$ (solid), and $Z' \to \mu\mu$ (dashed) for 800-GeV and 4-TeV $Z'$ masses. Figure 26 and 27 show the angular distributions for 800 (4000) GeV $Z'$ with the longitudinal momentum of the $Z'$ required to be $> 500$ (1000) GeV for a perfect detector (dotted), electron decay modes (solid), and muon modes (dashed). With adequate statistics, it is possible to measure the asymmetry and to distinguish among the models.

Table 2. Properties of Several $Z'$ Arising in $E_6$ Models.

| Property | $\cos\alpha = -0.6$ | $Z_\eta$ | $Z_\Psi$ | $Z_\chi$ | SM Couplings | |
|---|---|---|---|---|---|---|
| $\Gamma(M = 800$ GeV) | 8.5 | 5.0 | 4.2 | 9.2 | 21.4 | GeV |
| $\Gamma(M = 4000$ GeV) | 42.3 | 25.2 | 21.0 | 46.2 | 106.9 | |
| $\sigma(M = 800$ GeV) | 2.1 | 1.2 | 1.1 | 2.4 | 4.3 | pb |
| $\sigma(M = 4000$ GeV) | 0.004 | 0.0032 | 0.0027 | 0.0051 | 0.010 | (into $e^+e^-$) |

Other standard model extensions include searches for quark or lepton substructure. Such searches are performed by looking for deviations in the jet production cross section from the standard model prediction. Studies for SDC show that the detector should be able to set a limit on such substructure at about 30 TeV after one SSC year.

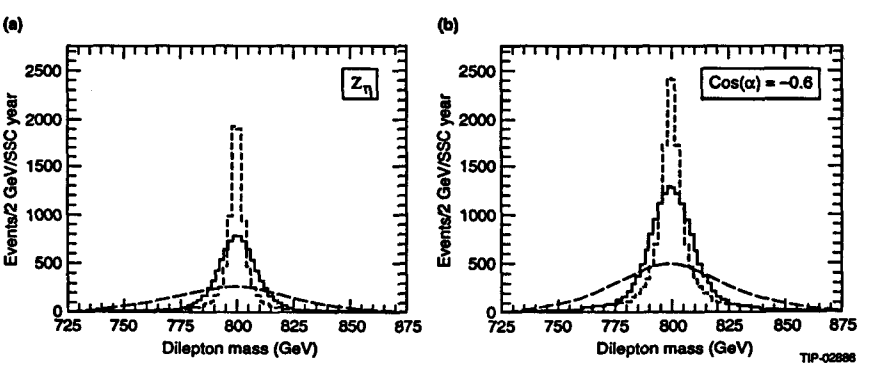


**Figure 24.** The cross section $d\sigma/dM$ for the production of an $\ell^+\ell^-$ pair for perfect resolution (dotted), the SDC resolution for electron pairs (solid), and the SDC resolution for muon pairs (dashed), as a function of the lepton pair invariant mass. The background is from the continuum production of lepton pairs (Drell-Yan). (a) The peak corresponds to a $Z_\eta$ with a mass of 800 GeV. (b) The peak corresponds to a new $Z$ with $\cos\alpha = -0.6$ and a mass of 800 GeV.

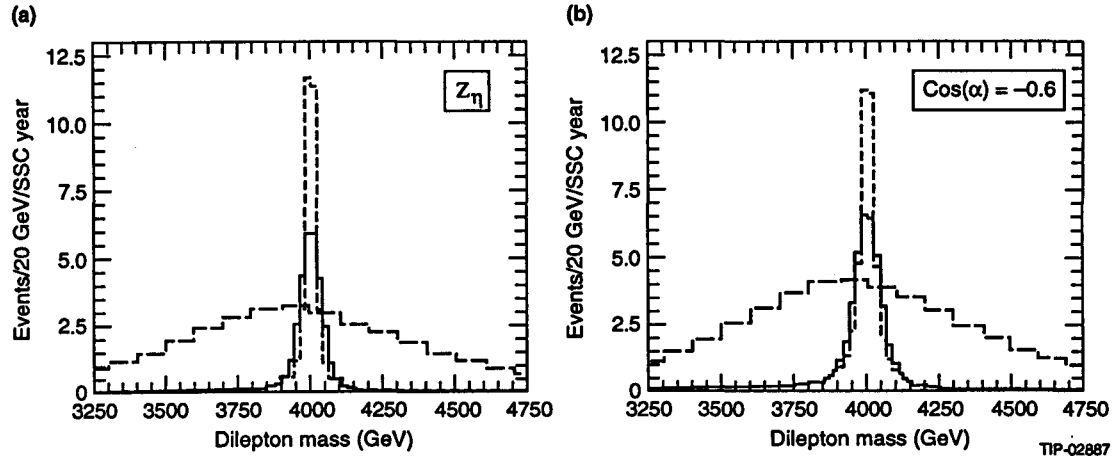


**Figure 25.** As Figure 24, except that the mass of the new $Z$ is taken to be 4000 GeV.

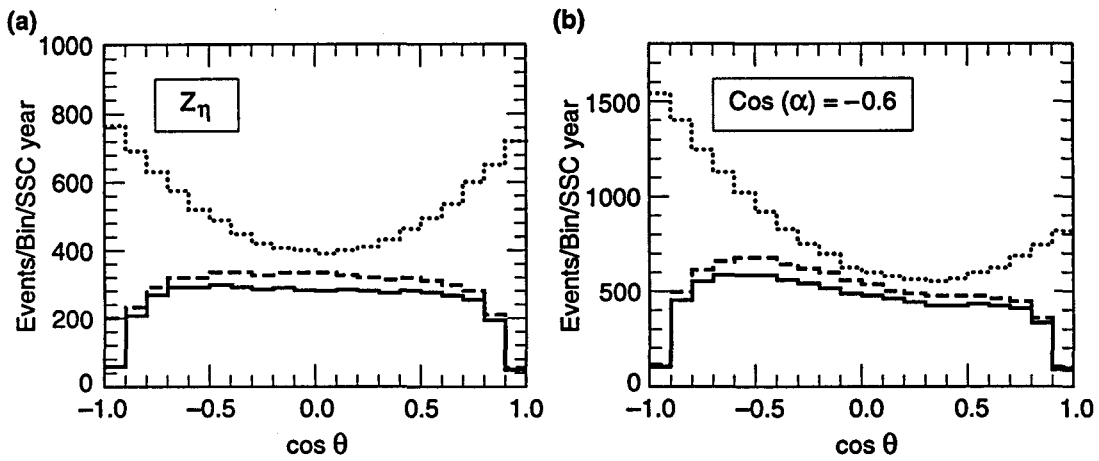


**Figure 26.** The cross section $d\sigma/d\cos\theta$ for the production of a lepton pair. The expected SDC result for $e^+e^-$ (Solid Curve) and $\mu^+\mu^-$ (Dashed Curve) is Shown. A perfect detector, which neglects acceptance and resolution smearing, is shown for reference (dotted curve). The reconstructed dilepton invariant mass is required to be between 700 and 900 GeV. The longitudinal momentum of the dilepton pair is required to be greater than 500 GeV. Events appear in the plot if the total charge of the lepton pair as determined by the detector is zero. (a) for a $Z_\eta$ with mass of 800 GeV. (b) for a new $Z$ with $\cos\alpha = -0.6$ and a mass of 800 GeV.

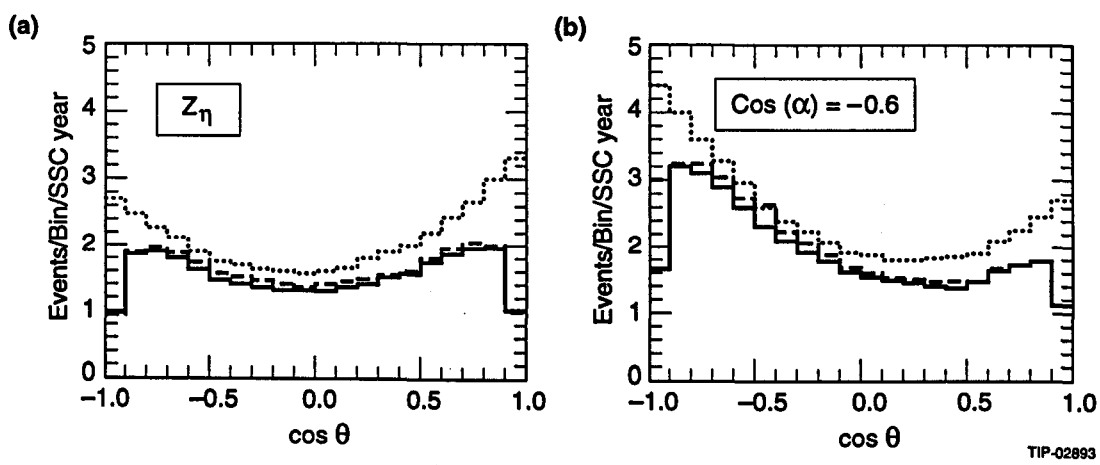


**Figure 27.** As Figure 26, except that a new $Z$ with a mass of 4000 GeV has been assumed. The invariant mass of the dilepton pair was required to be between 3000 and 4000 GeV, and the longitudinal momentum was required to be greater than 1000 GeV.

## BEYOND THE STANDARD MODEL

Many models propose frameworks that vastly extend the standard model picture. Supersymmetric models hypothesize an additional global symmetry that connects particles of differing spin. The minimal model ($N = 1$ supersymmetry) has a single generator $Q_\alpha$ that transforms as spin 1/2 under the Lorentz group. $Q_\alpha$ acting on an ordinary massless state of helicity $h$ generates a superpartner of helicity $h - 1/2$. Because of various commutation rules satisfied by $Q_\alpha$, when $Q_\alpha$ is applied again, the result vanishes. For this reason, the super multiplets are doublets, with two particles that differ by 1/2 unit of spin angular momentum. The super particles corresponding to the spin-1 gauge bosons are the spin-1/2 gauginos—gluino, wino, zino, and photino. The super particles corresponding to the spin-1/2 fermions are spin-0 partners to the quarks and leptons—squarks and sleptons.

Since $Q_\alpha$ commutes with the other operators, the quantum numbers of the super partners are the same as for the original particles, but they carry an additional quantum number $R$, that is absolutely conserved. Since supersymmetry is not readily seen in experiments, the symmetry must be broken. The conservation of $R$ implies that the lightest super partners must be stable. To help solve the "naturalness" problem, the expected scale of supersymmetric scale breaking should be of order $M_W$. Such models seem to be the best candidates to solve the mass hierarchy problem and to connect the standard model with gravity.

In the minimal supersymmetric model (MSSM), the scalar squarks and sleptons are denoted by $\tilde{q}$ and $\tilde{l}$. The fermionic partners of the gauge and Higgs fields are usually represented by the mass eigenstates indicated as $\tilde{g}$, $\tilde{\chi}_i^\pm$ ($i = 1,2$), $\tilde{\chi}_i^0$ ($i = 1,\ldots,4$). The scalar Higgs fields are $H^\pm$, $h^0$, $H^0$, and $A$. The parameters in the model are $\tan\beta$, the ratio of the vacuum expectation values of the Higgs doublets; $\mu$, the Higgs mass at the grand unified scale; scalar masses; and $M$, the common gaugino mass at the grand unified scale. There exists a lightest stable SUSY particle, $\tilde{\chi}_1^0$.

For SDC physics studies,[11] production of gluino pairs and their detection via decays to like-sign dileptons + jets ($\tilde{g}\tilde{g} \to l^\pm l^\pm + (n \geq 4)$ jets) and by missing $E_t$ in multi-jet events have been considered.

### Missing $E_t$

For the more difficult case of a light gluino, $M_{\tilde{g}} = 300$ GeV, with $m_{\tilde{q}} > m_{\tilde{g}}$, the gluino decays are dominated by the channels

$$\begin{aligned} \tilde{g} &\to \chi_1^\pm q\bar{q}' && (BR \sim 60\%) \\ \tilde{g} &\to \tilde{\chi}_1^0 q\bar{q} && (BR \sim 15\%) \\ \tilde{g} &\to \tilde{\chi}_2^0 q\bar{q} && (BR \sim 25\%), \end{aligned}$$

followed by subsequent decay of the $\tilde{\chi}$ to the stable state $\tilde{\chi}_1^0$:

$$\begin{aligned} \tilde{\chi}_1^\pm &\to \tilde{\chi}_1^0 + X \\ \tilde{\chi}_2^0 &\to \tilde{\chi}_1^0 + X, \end{aligned}$$

where $X$ contains at least a quark or lepton pair. To search for the signal, advantage is taken of the stability of $\tilde{\chi}_1^0$—which will simulate a neutrino—by looking at the missing $E_t$ spectrum in events with 3 or more jets with $p_t > 70$ GeV. The backgrounds to this process are $Z \to \nu\nu$+jets, heavy flavor quarks $\to \nu$+jets, jet energy mismeasurement, and jets lost outside the detector acceptance in the forward region. To reduce the impact of jet energy mismeasurement on the missing $E_t$ measurement, the azimuthal angle between the missing $E_t$ and the jets is required to be $> 20°$. Figure 28 shows the missing $E_t$ spectrum for calorimeter coverage to $\eta = 5$ with and without the azimuthal angle cut. As can be seen, the $\phi$ cut is needed to suppress background and has little influence on the signal. Figure 29 shows the impact of forward calorimeter coverage to $|\eta| = 4$ or 5. As can be seen coverage for jets to $|\eta| = 5$ is required. Figure 30 shows the result for the SDC design for signal and backgrounds.

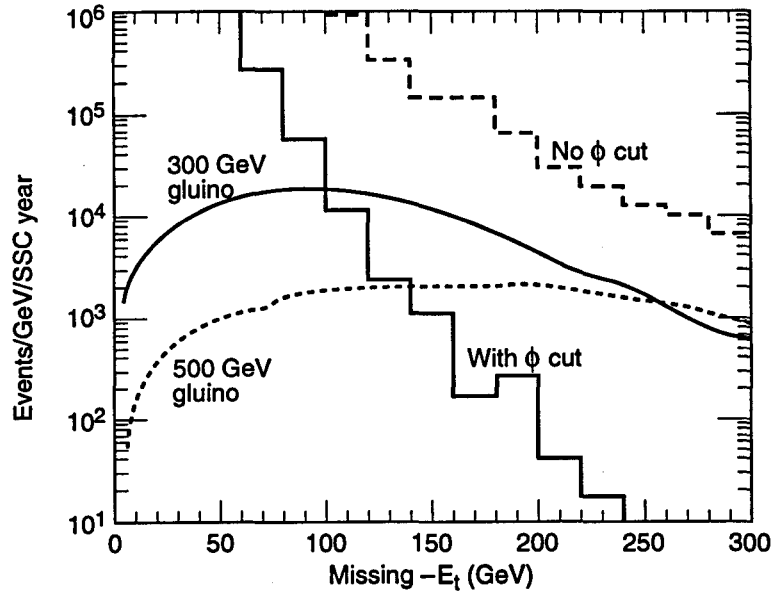


**Figure 28.** Comparison of the missing-$E_t$ distributions for the background (to light gluino pair production) due to multijet events with mismeasurement of a jet. The two histograms are with (solid) and without (dashed) a cut on events containing a jet with $E_t > 70$ GeV within an azimuthal angle of 40° of the missing-$E_t$. The events are required to have three or more jets each with $E_t > 70$ GeV and $|\eta| < 3$ separated by $\Delta R$ of 0.7. The solid (dotted) curve is for pair production of 300 GeV (500 GeV) gluinos decaying as described in the text.

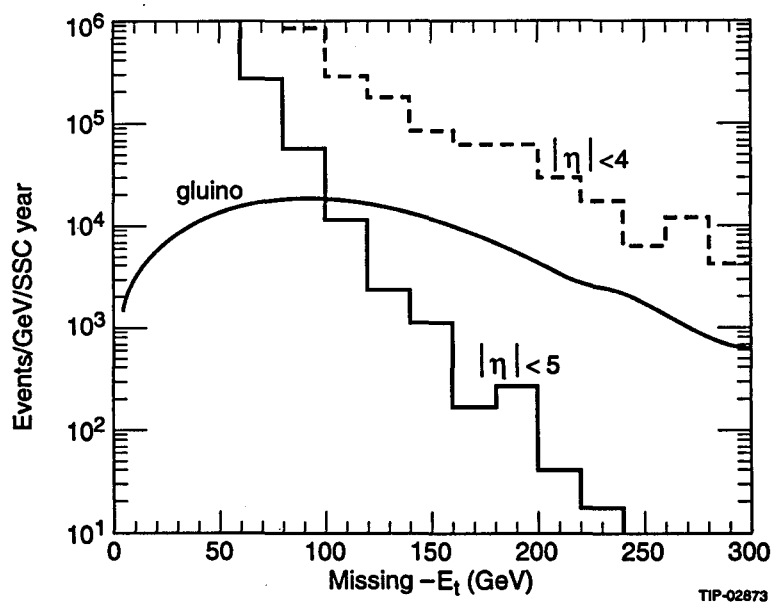


**Figure 29.** Comparison of the missing-$E_t$ distributions for the background (to light gluino pair production) due to multijet events with energy loss out of the end of the detector, $|\eta| > 4$ (dashed histogram) or 5 (solid histogram). The events are required to have three or more jets each with $E_t > 70$ GeV and $|\eta| < 3$ separated by $\Delta R = 0.7$. Events are rejected if they contain a jet with $E_t > 70$ GeV within an azimuthal angle of 40° of the missing-$E_t$. The solid curve is for pair production of 300 GeV gluinos decaying as described in the text.

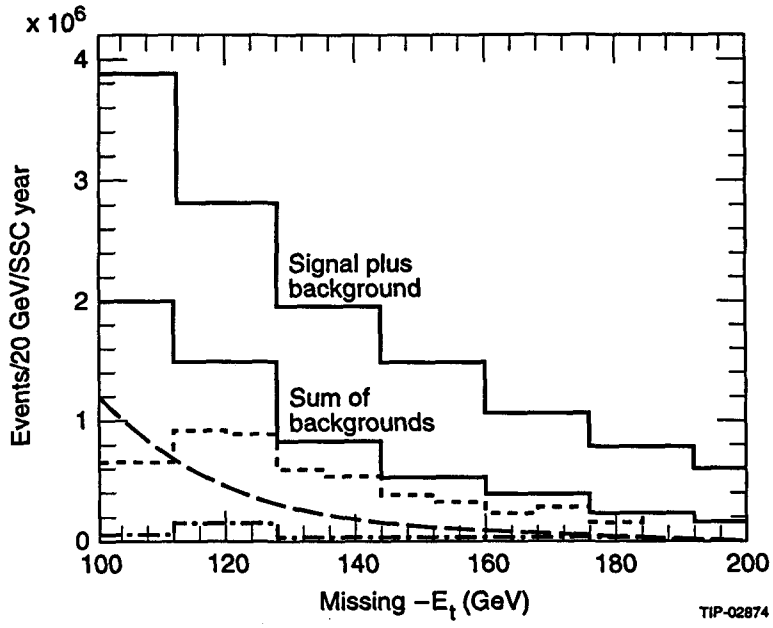


**Figure 30.** Search for evidence of gluino pair production in the distribution of missing-$E_t$ for the final state of three or more jets each with $E_t > 70$ GeV separated by $\Delta R = 0.7$. The jets are required to have $|\eta| < 5$. Events are rejected if they contain a jet with $E_t > 70$ GeV within an azimuthal angle of 20° of the missing-$E_t$ vector or if they have circularity $C < 0.2$. The signal is for pair productions of 300 GeV gluinos decaying as described in the text. The lower solid histogram is the sum of the individual background contributions, the upper solid histogram is the sum of the background and the gluino signal. The detector-dependent background due to multijet events with missing-$E_t$ generated by calorimeter resolution or by energy loss out of the end of the detector ($|\eta| > 5$) is shown as a dashed curve. The dotted background arises from the final states $t\bar{t}$ and $b\bar{b}$, where the missing-$E_t$ is due to neutrinos. The dash-dotted background is due to $Z +$ *multijet* events.

## Like-Sign Di-Leptons

In this mode, a search is made for the following decay chain for each $\tilde{g}$:

$$\tilde{g} \rightarrow \tilde{\chi}_1^{\pm} q\bar{q}' \qquad (BR \sim 60\%)$$
$$\tilde{\chi}_1^{\pm} \rightarrow l^{\pm}\nu\tilde{\chi}_1^0 \qquad (BR \sim 20\%).$$

The total $BR$ is about 2%, half of which corresponds to same-sign lepton pairs. This corresponds to $2 \times 10^6$-events (25 events) for $m_{\tilde{g}} = 180$ GeV (2 TeV). For the case $m_{\tilde{g}} = 300$ GeV, we require $\geq 4$ jets with $|\eta| < 3$ and $p_t > 50$ GeV, $p_t > 20$ GeV for both leptons, and $\Delta R$ between the lepton and jet $> 0.5$ to reduce the $t\bar{t}$ background. Figure 31 shows the mass of the lower-$p_t$ lepton and the two nearest jets for the signal and the top background *without* the separation cut. The top background is eliminated by the cut. Figure 32 shows the mass distributions for the high-$p_t$ lepton plus the two nearest jets for two different gluino masses. The mass resolution using this method is about 10%.

These and other studies[11] show that the SDC design will be capable of detecting gluinos in the range $180 < m_{\tilde{g}} < 0$ (TeV) using two independent decay channels. Supersymmetry will manifest itself in several different phenomena. The coincidence and consistency of the various signals will help select the particular model chosen by nature.

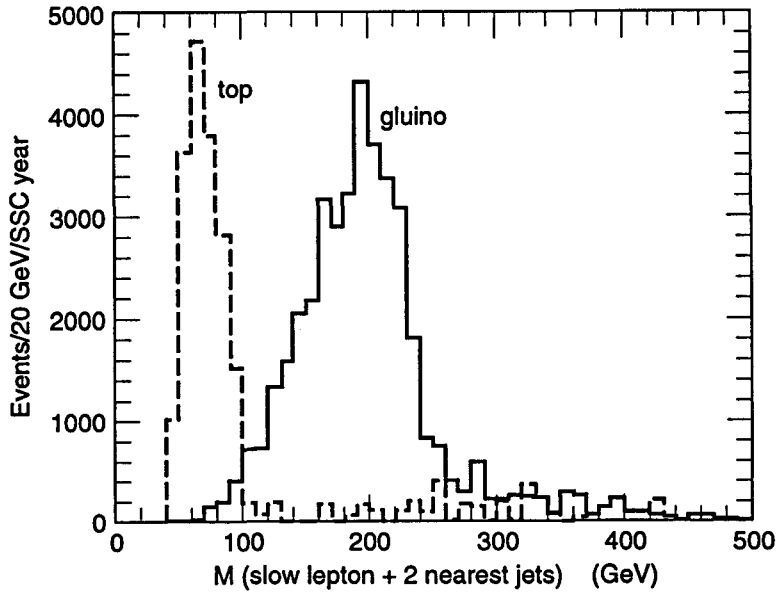


**Figure 31.** For events with two isolated same-sign leptons, the distribution of the invariant mass of the lower $p_t$ lepton together with the two nearest jets chosen from the four jets with the highest $p_t$. Each lepton is required to have $p_t > 20$ GeV or alternatively one lepton must have $p_t > 40$ GeV and the other $p_t > 15$ GeV. The leptons must lie within $|\eta| < 2.5$. Events are required to have at least four jets with $p_t > 50$ GeV. The gluino mass was taken to be 300 GeV. The solid histogram is from gluino pair production and decay ($\tilde{g}\tilde{g} \to q\bar{q}\tilde{\chi}_1^+ q\bar{q}\tilde{\chi}_1^+ \to q\bar{q}\ell^+\nu\tilde{\chi}_1^0 q\bar{q}\ell^+\nu\tilde{\chi}_1^0$), whereas the dashed curve is due to $t\bar{t}$ production and decay ($t\bar{t} \to b\ell^+\nu\bar{c}\ell^+\nu$ *jets*, with $M_{\rm top} = 150$ GeV). Unlike the signal, the dashed curve has not had any isolation cut applied. Such a cut would have eliminated it entirely.

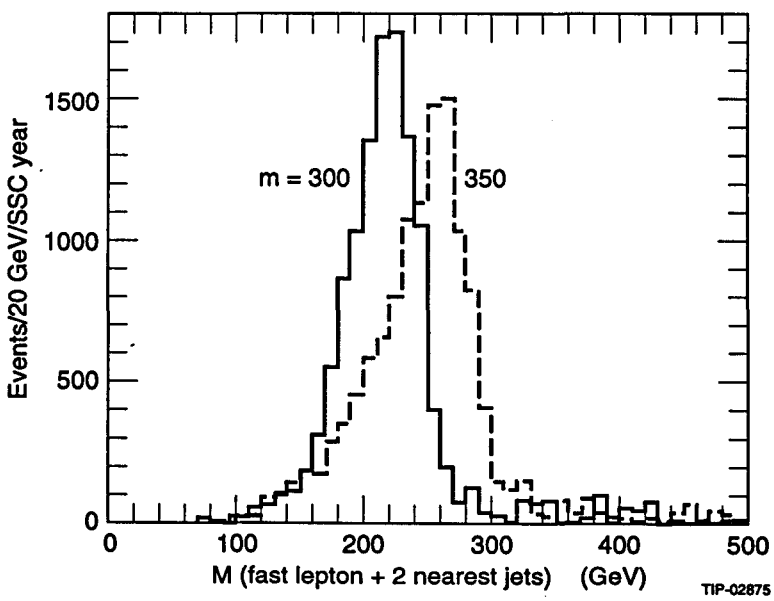


**Figure 32.** For events with two isolated same-sign leptons, the distribution of the invariant mass of the higher $p_t$ lepton together with the two nearest jets chosen from the four jets with the highest $p_t$. Events are required to have one lepton with $p_t > 15$ GeV, one with $p_t > 65$ GeV, and at least four jets with $p_t > 50$ GeV. The leptons must lie within $|\eta| < 2.5$. The solid (dashed) curve is from $M = 300$ GeV ($M = 350$ GeV) gluino pair production and decay. The 300 GeV (350 GeV) gluino yields 6000 events (12,000 events) per year. (The cross section rises quickly with mass because of our cuts). The dashed curve has been divided by two for display purposes. This calculation was done using a parton-level Monte Carlo including resolution; a more realistic calculation will add tails to the peaks due to radiated jets that accidentally are near the lepton.

## ELECTROWEAK SYMMETRY BREAKING

The theoretical notions concerning the nature of electroweak symmetry breaking reflect a wide range of ideas. The "conventional" picture involves one scalar particle that results when "spontaneous symmetry breaking"—a non-vanishing vacuum expectation value for the Higgs complex doublet field that selects a preferred direction in weak isospin and hypercharge space—breaks the $SU(2) \times U(1)$ symmetry of the standard model. The other three components of the Higgs field are combined with the transverse components of the gauge bosons in the unbroken theory to form the massive $W^{\pm}$ and $Z^0$ bosons. In minimal supersymmetric models, the situation is slightly more complicated, as two complex doublets are required for the Higgs field, yielding five remaining degrees of freedom denoted $h^0$, $H^0$, $A^0$ and $H^{\pm}$.

Deviations from this conventional picture, with fundamental Higgs scalars, are found in models in which scalar Higgs bosons exist, but they are composite particles, several neutral and charged, depending on the model. Such models (technicolor) require a new underlying force and new fermions to realize the symmetry-breaking sector.

In unconventional models, no Higgs bosons exist at all. Instead, the high-energy $W_L W_L$ interaction becomes non-perturbative, and the weak interactions become "strong" at high energy. In this case, resonances in gauge-boson scattering occur, and their effects can be seen even at SSC energies.

All these possibilities must be distinguished experimentally. To elucidate the nature of the electroweak symmetry-breaking sector is the main goal of the SSC experimental program. Much work has been done on the minimal standard model Higgs and its decay modes in various mass ranges. Details of the performance of the SDC design for this case and some results on supersymmetric models and $W_L W_L$ scattering follow.

### Minimal Standard Model Higgs

The dominant production mechanisms for the standard model Higgs versus Higgs mass at the SSC are shown in Figure 33. Production by gluon-gluon fusion via a heavy quark loop is shown in solid, by $WW$ or $ZZ$ fusion in dots, by associated production with a $t\bar{t}$ pair in dot-dash, and by associated production with a $W$ or $Z$ boson in dashes in Figure 33. The curves are shown for top-quark mass values of 100, 150, and 200 GeV. A top quark mass of 150 GeV will be used in all subsequent work.

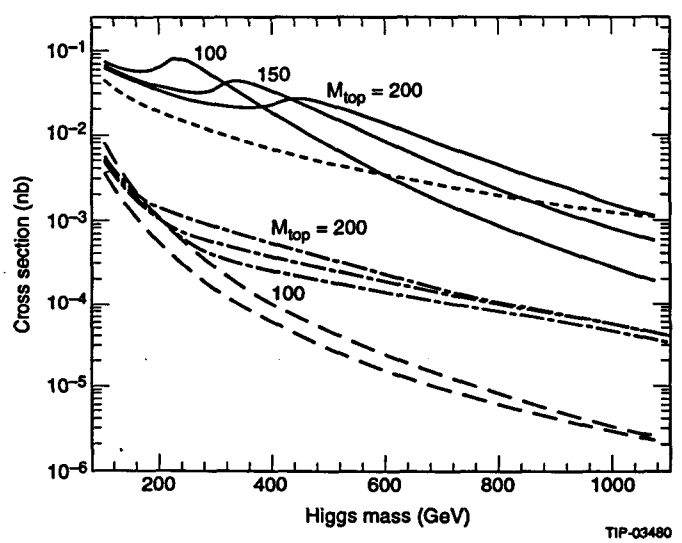


**Figure 33.** The cross section for the production of a Higgs boson in $pp$ collisions at $\sqrt{s} = 40$ TeV as a function of the Higgs boson mass for several different production mechanisms: $gg$ fusion (solid), $WW/ZZ$ fusion (dotted), $t\bar{t} + H$ production (dot-dashed), $W + H$ production (upper dashed), and $Z + H$ production (lower dashed). When the cross section depends on the $t$-quark mass, several curves have been included for different values of $M_{\text{top}}$.

The decay modes of the standard Higgs are shown in Figure 34. For masses below the $WW$ and $ZZ$ threshold, the Higgs boson is very narrow (see Table 3), while at the highest masses it becomes quite broad. For good behavior of the lowest-order diagrams involving the Higgs, the Higgs is expected to be have mass less than $\sim 1$ TeV. Note from Figure 34 that decays $H \rightarrow ZZ^*$ or $ZZ$ are significant for Higgs masses above approximately 140 GeV. Note also the small but significant $H \rightarrow \gamma\gamma$ branching ratio below 160 GeV. For the purpose of analysis, we divide the mass ranges into low mass ($80 < m < 130$ GeV), intermediate mass ($130 < m < 180$ GeV), and high mass ($> 180$ GeV).

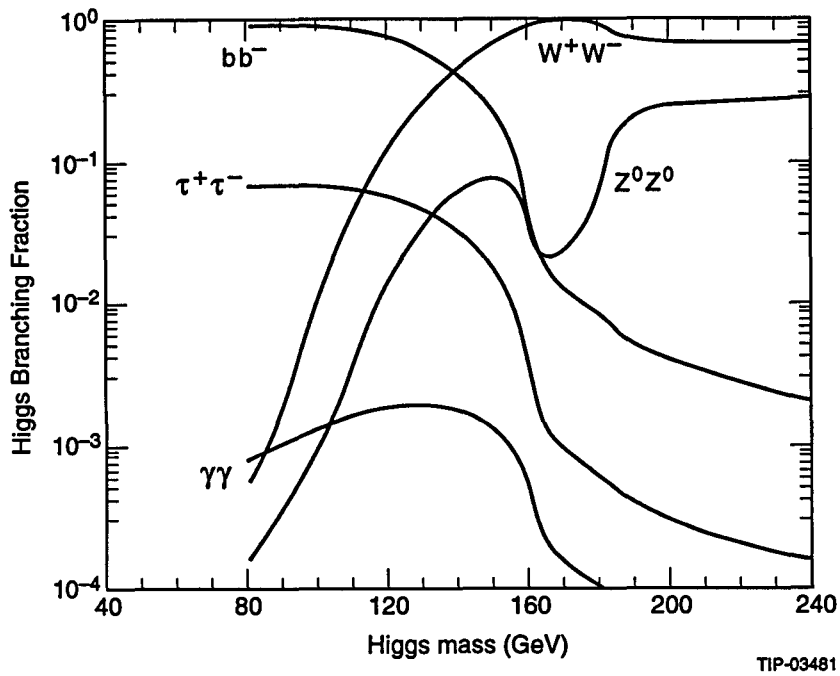


**Figure 34.** The branching ratio for a Higgs boson into various channels as a function of its mass.

Table 3. Decays of Standard Model Higgs.

| Higgs Mass (GeV) | Higgs Width (GeV) |
|---|---|
| 140 | 0.01 |
| 160 | 0.1 |
| 200 | 1.4 |
| 400 | 30 |
| 800 | 270 |

## Low Mass Higgs

Searches at LEP-II are unlikely to extend much above 80 GeV, due to statistics and backgrounds from $ZZ$ production. Direct production in $pp$ collisions of $H \rightarrow \gamma\gamma$ suffers from a large continuum background from QCD production of photon pairs and misidentified 2-jet events. In addition, good mass resolution requires accurate knowledge of photon directions. For the SDC design, the signals for $M_H = 80$, 100, 120, 140, and 160 GeV are shown along with the background in Figure 35. (Only backgrounds from QCD photon pair production are included.) Figure 36 shows the result when a smooth two-photon background is subtracted in order to study the significance of signals. The significance of this marginal signal would increase slowly with improved calorimeter resolution, but the prohibitive cost of achieving the needed

resolution suggests that other modes suffering less background would be more suitable for the SDC design.

Associated production of Higgs with a $W$ or $t$ quark gives an additional lepton tag that assists with triggering and significantly reduces the background. Figure 37 shows the efficiency for detection of $t\hat{t} + H \rightarrow l\gamma\gamma + X$ vs. $p_t$ and $\eta$. The analysis requires $p_t > 20$ and $|\eta| < 2.5$ for the lepton and both photons. The dotted (solid) curves are for $M = 80$ (160) GeV, with four curves for $\eta$ coverage of 1.5, 2.0, 2.5, 3.0. Several classes of background have been considered in this process. These include two-photon backgrounds $W + \gamma\gamma$, $b\bar{b} + \gamma\gamma$, $t\bar{t} + \gamma\gamma$; QED radiative decays $W$, $Z + \gamma\gamma$, and leptons faking $\gamma$ in $Z + \gamma$; backgrounds with one real $\gamma$ and one misidentified jet ($t\bar{t} + \gamma$); and backgrounds where both photons arise from misidentified jets. Figure 38 shows the resulting estimated background vs. Higgs mass. Figure 39 shows the signal and background for associated light Higgs production with signals at 80, 100, 120, 140, and 160 GeV. Note that the right-hand scale shows the number of events expected; the curves are generated with large statistics. This signal can be confirmed by SDC after several years' running.

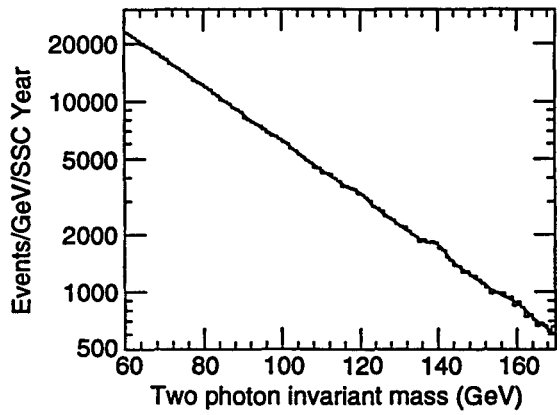


**Figure 35.** The two-photon invariant mass distribution including the signals from Higgs bosons with masses of 80, 100, 120, 140, and 160 GeV. The background includes only the irreducible backgrounds arising from the $q\bar{q} \rightarrow \gamma\gamma$ and $gg \rightarrow \gamma\gamma$ processes.

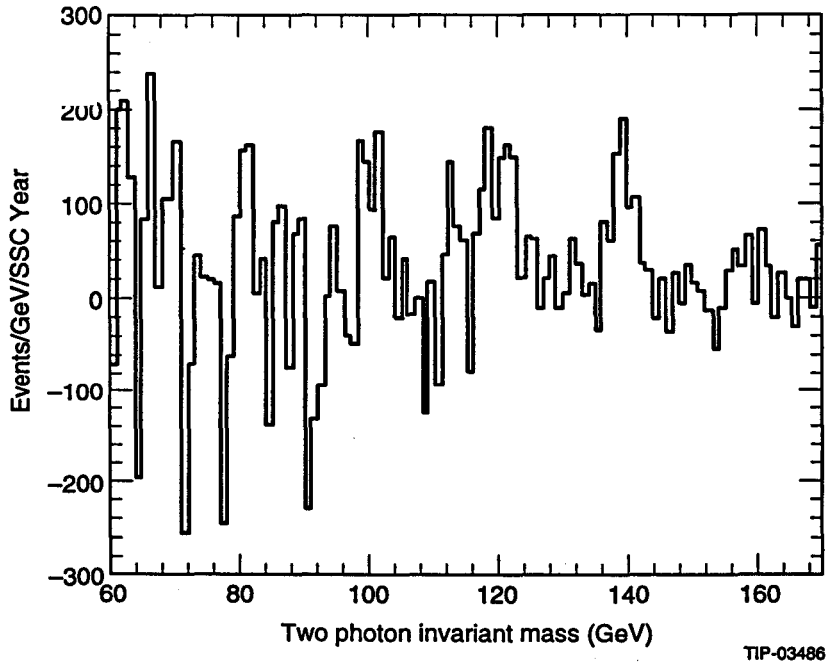


**Figure 36.** The expected signals from Higgs bosons with masses of 80, 100, 120, 140, and 160 GeV. The irreducible backgrounds displayed in Figure 35 have been statistically subtracted using an exponential fit to the background shape. The baseline calorimeter performance has been assumed.

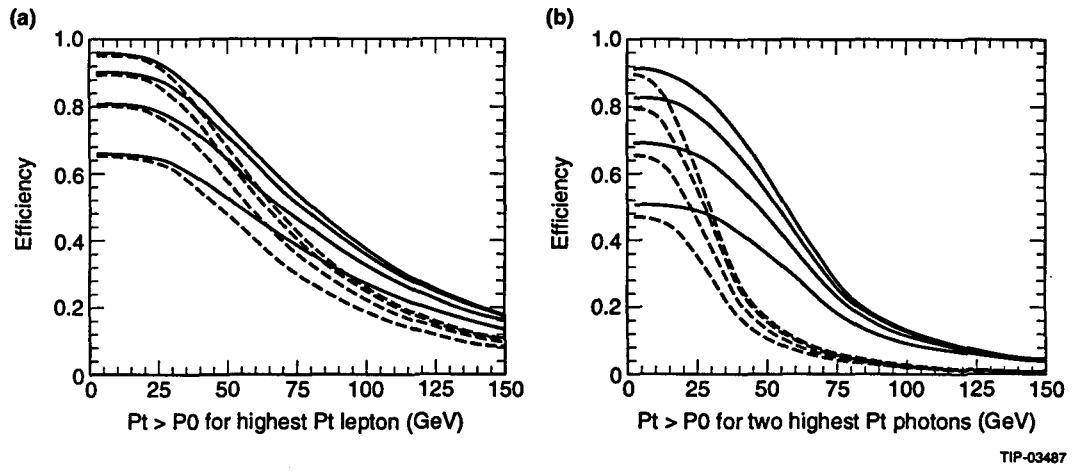


**Figure 37.** Families of acceptance curves for $t\bar{t} + H$, with $M_{\text{Higgs}} = 80$ GeV (dashed) and $M_{\text{Higgs}} = 160$ GeV (solid). (a) The fraction of events with at least one lepton with $p_t > p_0$ as a function of $p_0$. The lepton has $|\eta| < 1.5$ (lowest curve), 2.0 (lower middle curve), 2.5 (upper middle curve), or 3.0 (upper curve). (b) The fraction of events with at least two photons with $p_t > p_0$ as a function of $p_0$. The photons have $|\eta| < 1.5$ (lowest curve), 2.0 (lower middle curve), 2.5 (upper middle curve), or 3.0 (upper curve).

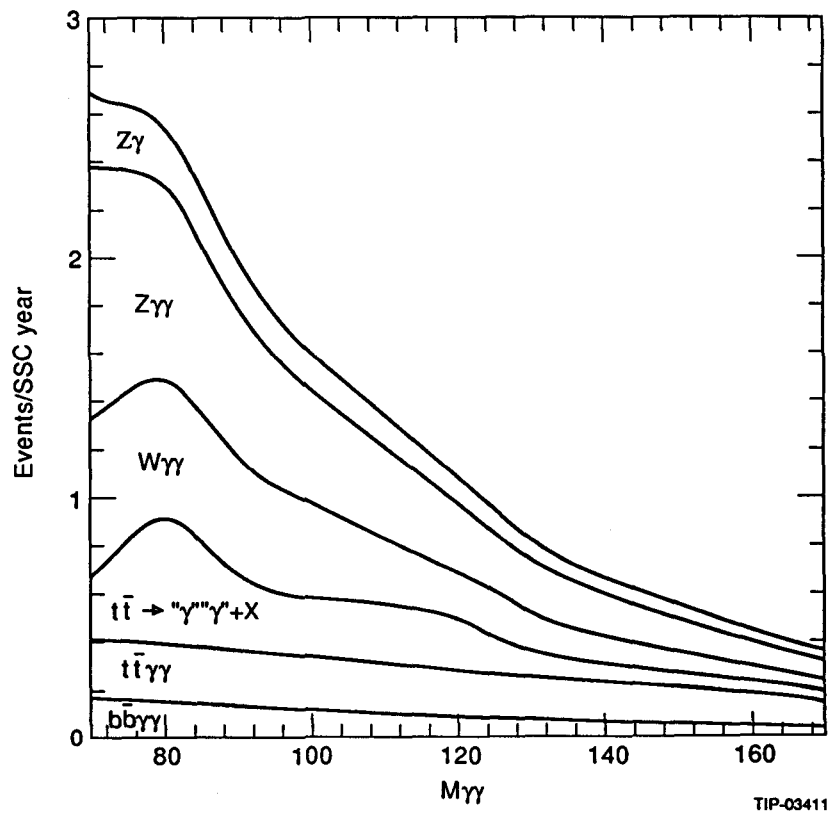


**Figure 38.** Backgrounds to $t\bar{t}$+ Higgs and $W$+ Higgs final state.

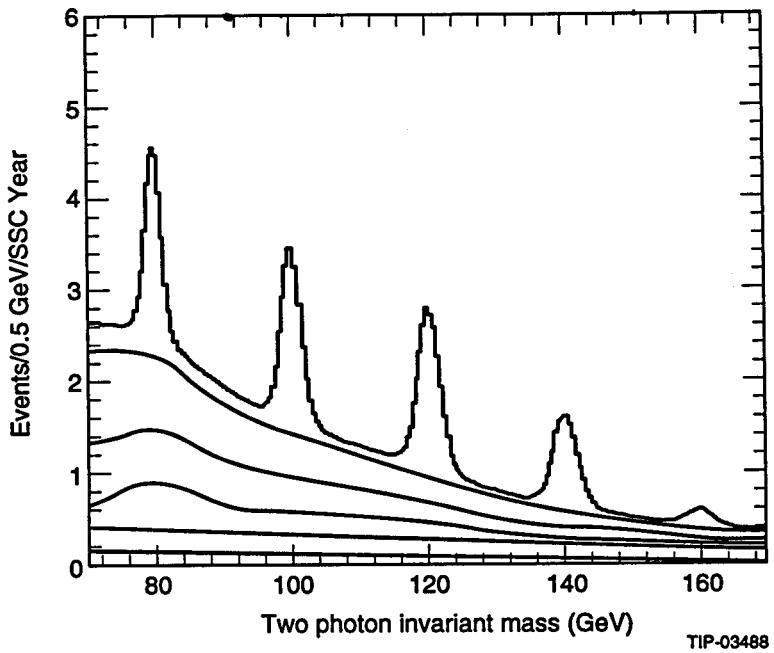


**Figure 39.** The two-photon invariant mass distribution for the expected signals from Higgs bosons of mass 80, 100, 120, 140, and 160 GeV. The background curves are cumulative, and are as shown in Figure 38. The baseline detector resolution has been assumed.

## Intermediate Mass Higgs

In this mass region, the decay $H \rightarrow ZZ^* \rightarrow 4l$ provides a distinctive signature. The efficiency for $H \rightarrow ZZ^*$ detection versus $p_t$ and $\eta$ is shown in Figure 40. The curves are for $M_H = 120$ GeV (solid), 140 GeV (dotted) and 160 GeV (dashed). The four curves are for $\eta$ coverages of 1.5, 2.0, 2.5, and 3.0. The $p_t$ for two leptons is $> 20$ GeV, and all four must be $> 10$ GeV with $|\eta| < 2.5$.

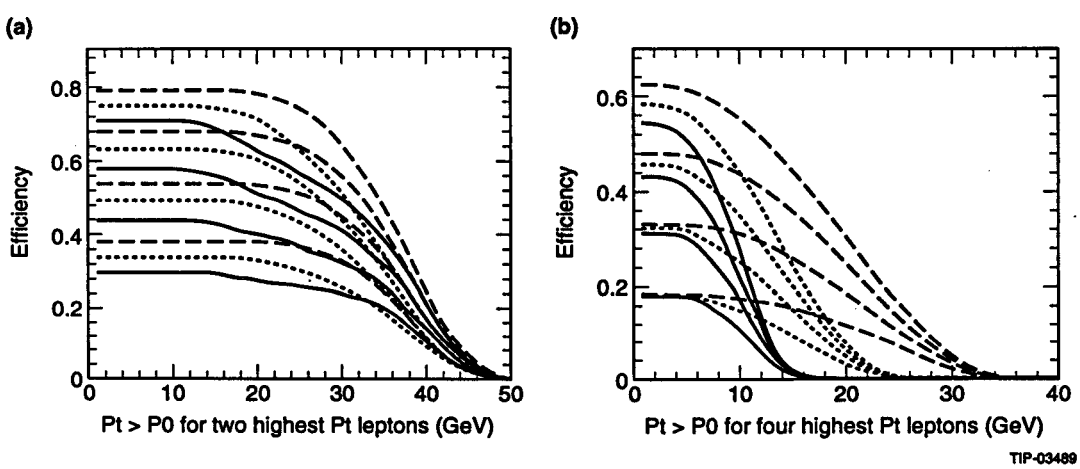


**Figure 40.** Families of acceptance curves for $H \rightarrow ZZ^*$, for $M_{\text{Higgs}} = 120$ GeV (solid), 140 GeV (dotted), and 160 GeV (dashed). (a) The fraction of events with at least two leptons with $p_t > p_0$ as a function of $p_0$. Both leptons have $|\eta| < 1.5$ (lower curve), 2.0 (lower middle curve), 2.5 (upper middle curve), or 3.0 (upper curve). (b) The fraction of events containing two leptons with $p_t > 20$ GeV and $|\eta| < 2.5$ plus two others with $p_t > p_0$ and $|\eta| < 1.5$ (lower curve), 2.0 (lower middle curve), 2.5 (upper middle curve), or 3.0 (upper curve).

Again, several classes of background have been considered. These include continuum $ZZ$ production from $q\bar{q}$ and $gg$ initial states where the latter has been approximated by scaling the former by 1.65, production of $Z + b\bar{b}$ and $Z + t\bar{t}$ with the heavy flavor decay providing two additional leptons, and production of $t\bar{t}$ with subsequent decay to four leptons. Topological requirements are effective at reducing the $t\bar{t}$ backgrounds. Figure 41 shows the distribution of excess $E_t$ in a cone of radius 0.3 around the leptons for $H \rightarrow ZZ^*$, and the $t\bar{t}$ backgrounds. Leptons from $b$ and lighter quark decays can be strongly suppressed while retaining high signal efficiency by requiring excess $E_t < 5$ GeV. This requirement is 94% efficient for signal leptons. Figure 42 shows the signal for Higgs masses of 130, 140, 150, 160, and 170 GeV, along with the background. For masses above 130 GeV, the signal will be visible in one SSC year.

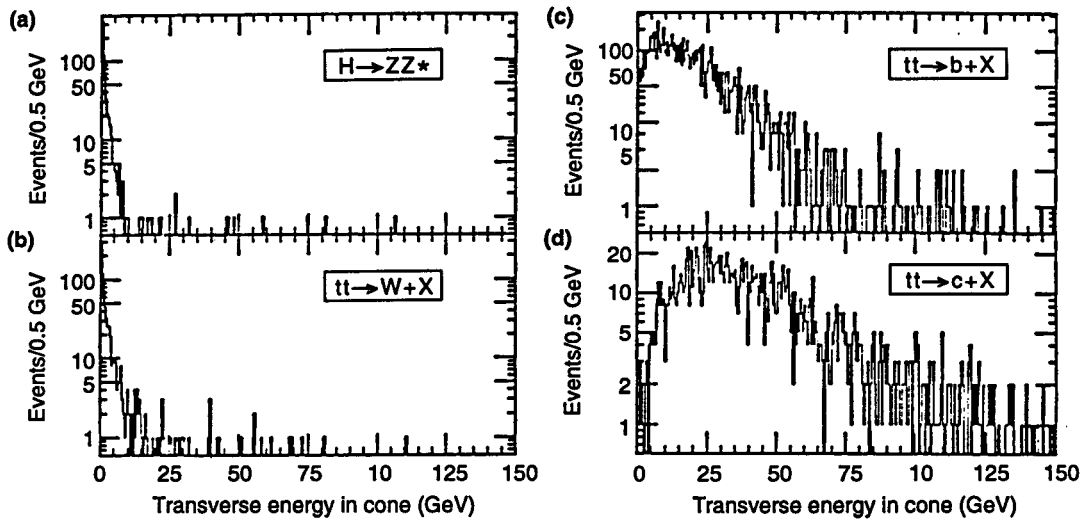


**Figure 41.** The distribution of excess $E_t$ in a cone of radius $R = 0.3$ for different classes of electrons. The electrons are all in the range $10 < p_t < 20$ GeV. (a) Electrons from $H \rightarrow ZZ^*$ for $M_{\text{Higgs}} =$ 140 GeV. (b) $W$ electrons coming from $t$ quark decays ($M_{\text{top}} = 150$ GeV). (c) $b$ electrons coming from $t$ quark decays. (d) $c$ (or $u$, $d$) electrons coming from $t$-quark decays.

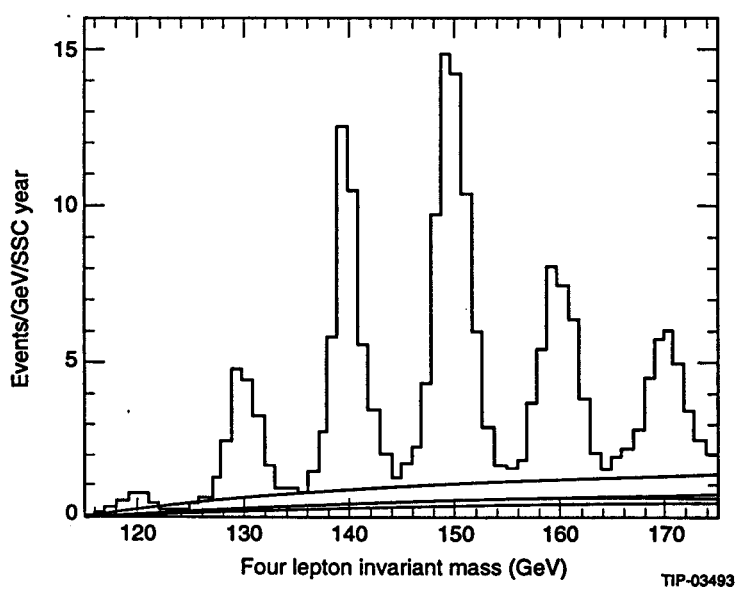


**Figure 42.** The reconstructed Higgs mass for $ZZ^*$ decaying to $4e$, $4\mu$, and $2e2\mu$ with $M_{\text{Higgs}} = 120$, 130, 140, 150, 160, and 170 GeV, including the expected backgrounds. The backgrounds curves are cumulative, and are (from lowest to highest): $q\bar{q} \rightarrow ZZ^*$, multiplied by 1.65 to account for $gg \rightarrow ZZ^*$, $Z + b\bar{b}$, $Z + t\bar{t}$, and $t\bar{t}$. The invariant mass has been calculated using calorimeter measurements for the electrons.

## Heavy Higgs

Clean but statistically limited modes $H \to ZZ \to 4l^{\pm}$ and $H \to ZZ \to 2l^{\pm}\nu\bar{\nu}$ have been considered in detail by SDC. Other modes with larger branching fractions are accompanied by much larger backgrounds. Figure 43 shows the efficiencies for $H \to ZZ \to 4l^{\pm}$ detection vs. $p_t$ and $\eta$. Results are for $M_H = 200$ (solid), 400 (dotted) and 800 (dashed) GeV. The four curves are for $\eta$ coverage of 1.5, 2.0, 2.5 and 3.0. The analysis requires $p_t > 20$ GeV for two leptons, and $p_t > 10$ GeV and $|\eta| < 2.5$ for all four leptons. The backgrounds are the same as those discussed previously for the $ZZ^*$ mode, but the second $Z$ mass constraint eliminates all but the $ZZ$ continuum background. Figure 44 (45) shows the expected signal along with the continuum background for Higgs of mass 200 and 400 (800) GeV. Since the statistics are not high in the 800-GeV sample, a cut requiring $p_t(Z) > 200$ GeV was applied that reduces the background with little effect on the signal. With this cut, about 14 signal events above a background of 6 events are expected for one SSC year.

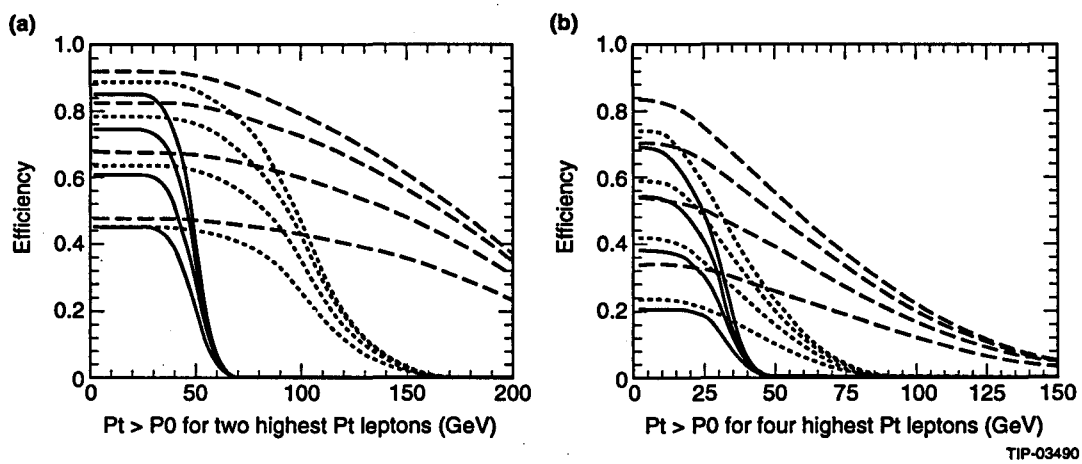


**Figure 43.** Families of acceptance curves for $H \to ZZ$, for $M_{\text{Higgs}} = 200$ GeV (solid), 400 GeV (dotted), and 800 GeV (dashed). (a) The fraction of events with at least two leptons with $p_t > p_0$ as a function of $p_0$. Both leptons have $|\eta| < 1.5$ (lower curve), 2.0 (lower middle curve), 2.5 (upper middle curve), or 3.0 (upper curve). (b) The fraction of events containing two leptons with $p_t > 20$ GeV and $|\eta| < 2.5$ plus two others with $p_t > p_0$ and $|\eta| < 1.5$ (lower curve), 2.0 (lower middle curve), 2.5 (upper middle curve), or 3.0 (upper curve).

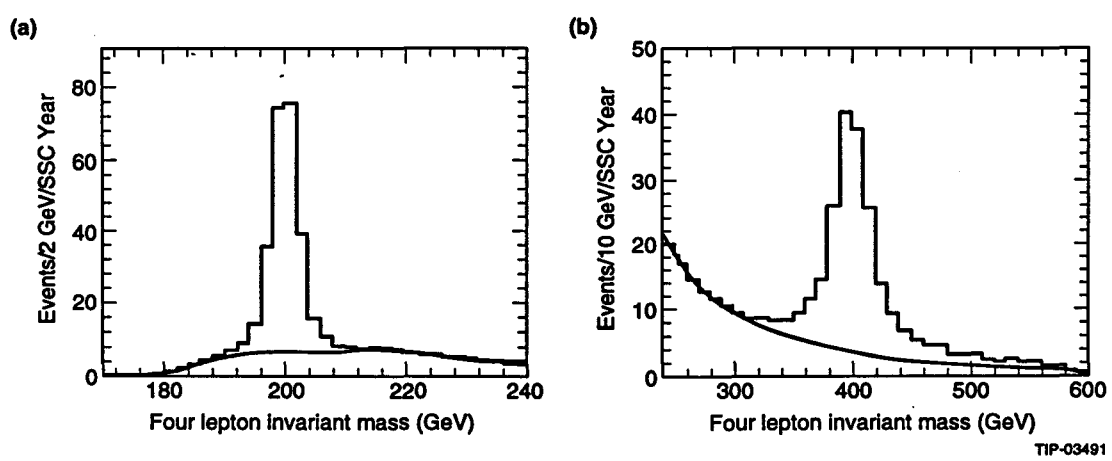


**Figure 44.** (a) The $ZZ$ invariant mass distribution showing a peak due to a Higgs of mass 200 GeV. The two lepton pairs were both required to have $M_{ll} = M_Z \pm 10$ GeV. The background curves have the same significance as those of Figure 42, but the $ZZ$ continuum background gives the only visible contribution. (b) Same as (a), except that the Higgs mass is 400 GeV.

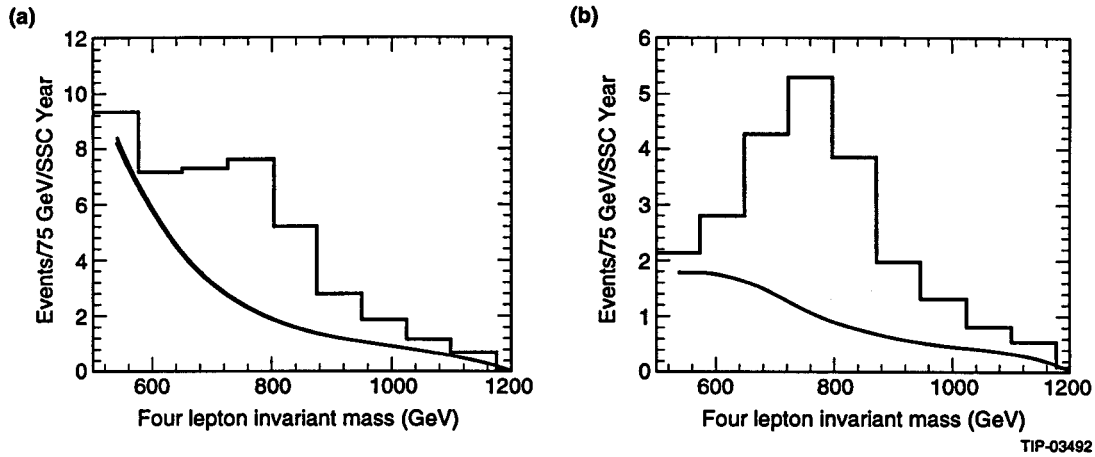


**Figure 45.** (a) Same as Figure 44(a), except that the Higgs mass is 800 GeV. (b) Same as (a), except that both $Z$'s were required to satisfy $p_t(Z) > 200$ GeV.

To improve on the rate at high mass, the mode $H \to ZZ \to 2l^{\pm}\,\nu\bar{\nu}$ was considered. The branching ratio is a factor six larger than the previous case, but the $2\nu$ mode is more sensitive to background. The major additional background is $Z+$ jets, where the $Z \to l^{\pm}l^{\mp}$, and one of the jets is mismeasured or lost to simulate the neutrinos. Continuum $ZZ$ production and production of $Z + b\bar{b}$ and $Z + t\bar{t}$ also contribute to the background. Figure 46 shows the expected number of events as a function of the missing $E_t$ in the events for the signal and background. The dashed line is the continuum background, the dot-dashed line is $Z+$ jets, and the dotted line is $Z + t\bar{t}$. This signal, in combination with the $4l^{\pm}$ final state, would provide strong evidence for an 800-GeV Higgs in one SSC year.

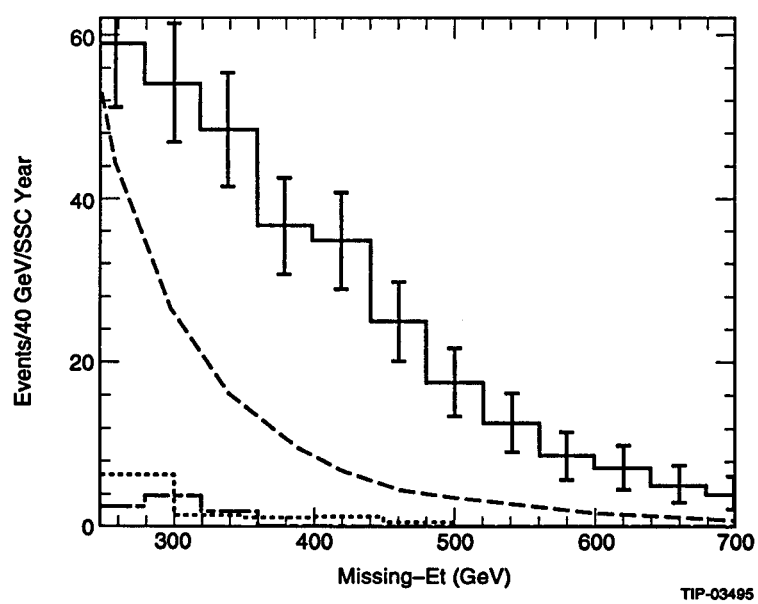


**Figure 46.** The distribution (solid histogram) in missing-$E_t$ for the final state $Z(\to \mu^+\mu^-, e^+e^-)+$ missing-$E_t$ including the effect of a Higgs boson of mass 800 GeV and the various backgrounds. The reconstructed $Z$ is required to have $p_t > 250$ GeV and the events are rejected if they contain a jet with $E_t > 300$ GeV. The background shown as a dashed curve arises from $q\bar{q} \to ZZ$ (multiplied by 1.65 to account for the $gg \to ZZ$ process). The dot-dashed background arises from the final state $Z +$ *jets* where the missing-$E_t$ is generated by calorimeter resolution or by losing energy out of the end of the detector. The dotted background arises from the final state $t\bar{t}$ where there is an $e^+e^-$ (or $\mu^+\mu^-$) pair of mass $M_Z \pm 20$ GeV and the missing-$E_t$ is due to neutrinos; the $Z + Q\bar{Q}$ background is negligible in this figure.

## Electroweak Symmetry Breaking in SUSY Models

The nature of SUSY models was outlined in a previous section. As was shown, evidence for supersymmetry would first be seen in relatively high-rate gluino production. Once SUSY is seen there, a more complicated Higgs sector would naturally be expected. The richer Higgs spectrum predicted in such models is a considerable experimental challenge to disentangle from the data. Extensive work with detailed detector simulations on the SUSY Higgs sector has not yet been carried out by the community. In the SDC case, decay modes of $\gamma\gamma$, $ZZ^*$, or $ZZ$, and top decay to charged Higgs have been studied. (Recall that for the two-doublet SUSY Higgs case, there are five physical Higgs bosons, $h^0$, $H^0$, $A^0$, and $H^\pm$.) The two free parameters are taken to be $M_A$ and $\tan\beta$, where $\beta$ is the ratio of the vacuum expectation values for the two Higgs doublets.

The branching ratios for neutral Higgs decays to $\gamma\gamma$ are shown in Figure 47, where the solid curve is for $h^0$ and the dotted (dashed) curve is for $H^0$ ($A^0$). For large values of $M_h^0$, $h^0 \to \gamma\gamma$ is observable. For small $\tan\beta$, $A^0 \to \gamma\gamma$ should be observable. Figure 48 shows the branching ratios for neutral Higgs to $ZZ$. Again, the solid curve is for $h^0$, and the dotted (dashed) curve is for $H^0$ ($A^0$). For large values of $\tan\beta$, $H^0 \to ZZ$ is observable. For small values of $\tan\beta$, $H^0 \to ZZ$ is observable. Studies of top $\to H^+b$ have shown that the charged Higgs can be seen for all values of $\tan\beta > 0.1$ via the $c\bar{s}$ and $\tau\nu_\tau$ decay modes.

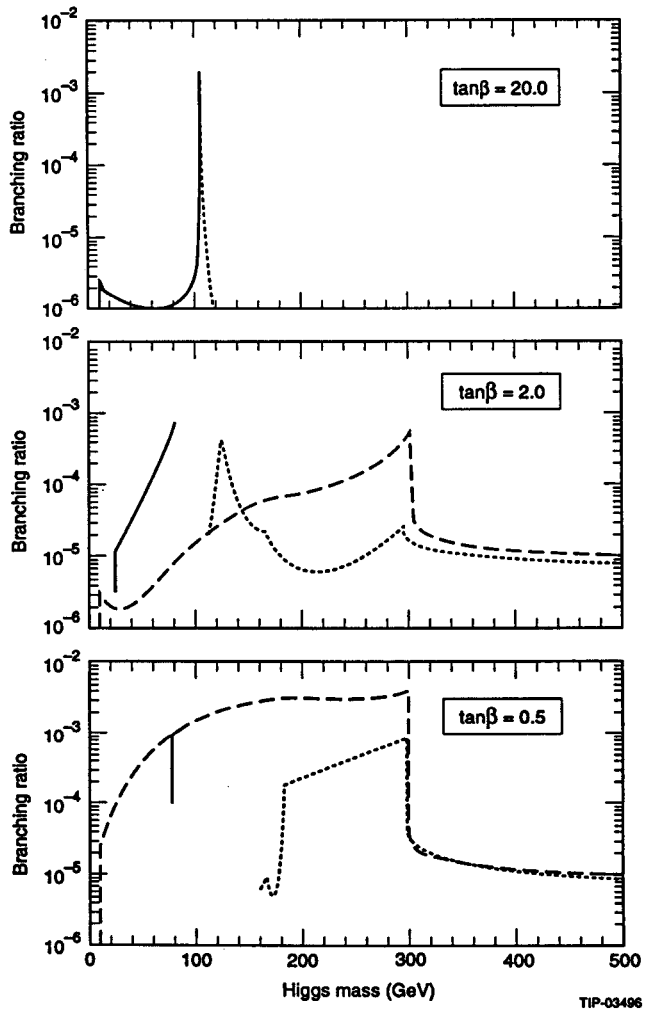


**Figure 47.** The branching ratios for the decay of the neutral Higgs bosons in the MSSM to the $\gamma\gamma$ final state, assuming $M_{\text{top}} = 150$ GeV. The solid curve is for the $h^0$, the dotted curve is for the $H^0$, and the dashed curve is for the $A^0$. The three different plots are for $\tan\beta = 0.5$, 2, and 20.

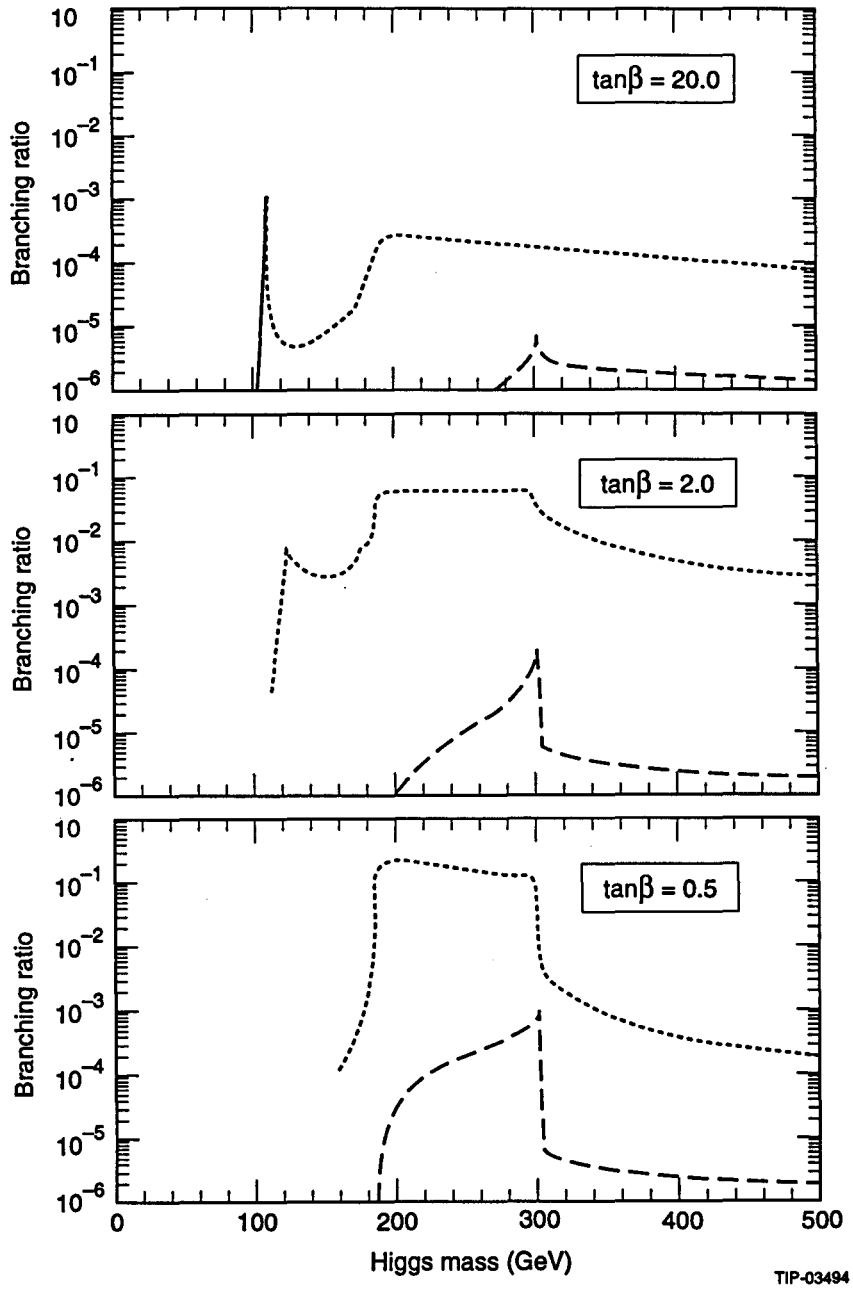


**Figure 48.** The branching ratios for the decay of the neutral Higgs bosons in the MSSM to the $ZZ$ or $ZZ^*$ final state, assuming $M_{\rm top} = 150$ GeV. The solid curve is for the $h^0$, the dotted curve is for the $H^0$, and the dashed curve is for the $A^0$. The three different plots are for $\tan\beta = 0.5$, 2, and 20.

Assuming 3–5 years at SSC design luminosity, the experimental situation can be summarized for SDC by the following comments. For small $M_A$, $h^0$ is observable at LEP-II, and $t \to H^{\pm}b$ is observable at SSC. For moderate $M_A$ and small $\tan\beta$, $h^0$ is observable at LEP-II, and $H^0 \to ZZ$, $t \to H^{\pm}b$ are observable at SSC. For moderate $M_A$ and large $\tan\beta$, none of the Higgs bosons may be observable in $ZZ$ or $\gamma\gamma$. For large $M_A$, $h^0 \to \gamma\gamma$ is observable at SSC.

Clearly, the experimental situation needs further work and clarification within the context of realistic detector models. Tau decays and $b$ tagging may provide some of the tools necessary to further extend the parameter range over which a viable search may be carried out.

## Strongly Coupled Models

If the Higgs mass is $\lesssim$1.8 TeV, the longitudinal $W$ scattering (Figure 49) process has good high-energy behavior—the cross section growth from lower energies is cut off by the exchange of narrow spin zero bosons (the Higgs). However, if $M_H \geq$ 1 TeV, the interaction of the longitudinal $W$ bosons (represented by the interaction lagrangian $\mathcal{L}_H$ in Figure 49) becomes strong, and a complex spectrum of particles and resonances is likely to appear. Such resonances are expected to be in the mass range 1–3 TeV. Even though the resonances may be too heavy to be directly detected at SSC, the interaction lagrangian $\mathcal{L}_H$ can still be probed via study of $WW$ scattering.

Resonant production also occurs in specific models such as technicolor models. Figure 50 shows the expected signal for a Techni-$\omega$ decaying to $Z\gamma$ in SDC. As can be seen, the signal is distinctive, but the low event rate means that high luminosity is required to see the signal.

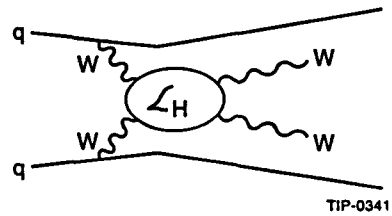


**Figure 49.** Schematic of $WW$ scattering, showing the interaction Lagrangian $\mathcal{L}_H$.

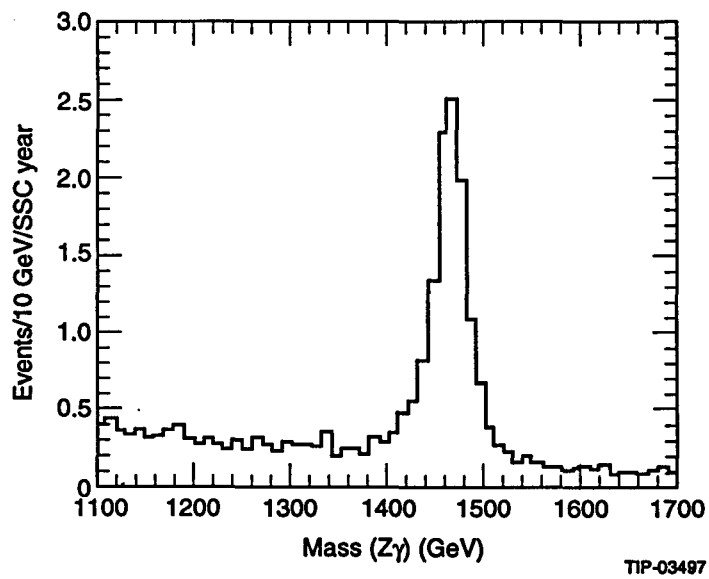


**Figure 50.** The distribution of invariant mass for the final state system of a photon and an $e^+e^-$. The lepton pair is required to have mass $M_Z \pm 10$ GeV. The leptons have $|\eta| < 2.5$ and the photon has $|\eta| < 3.0$. The peak corresponds to the production and decay of the techni-omega particle of mass 1.46 TeV discussed in the text.

Non-resonant $WW$ scattering has also been studied by SDC. The solid curve of Figure 51 shows the expected signal in a strong-coupling model due to Chanowitz.[15] The major experimental backgrounds, $q\bar{q} \rightarrow W^+W^-$ (dotted) and $gg \rightarrow t\bar{t} \rightarrow W^+W^- + X$ (dashed), are also shown. To suppress these backgrounds, same-sign $W$ pairs may be used; the like-sign backgrounds from $gg \rightarrow t\bar{t} \rightarrow W + b\bar{b} + X \rightarrow l^+l^+ + X$ are also shown (dot-dashed) in Figure 51.

Clearly, accurate charge measurement is critical to carry out this measurement. For $p_t$ of the lepton of 100 (500) GeV, rejection of the opposite sign background of $10^{-5}$ ($10^{-3}$) is needed. The like-sign $t\bar{t}$ events are relatively easily rejected by means of isolation cuts on the leptons.

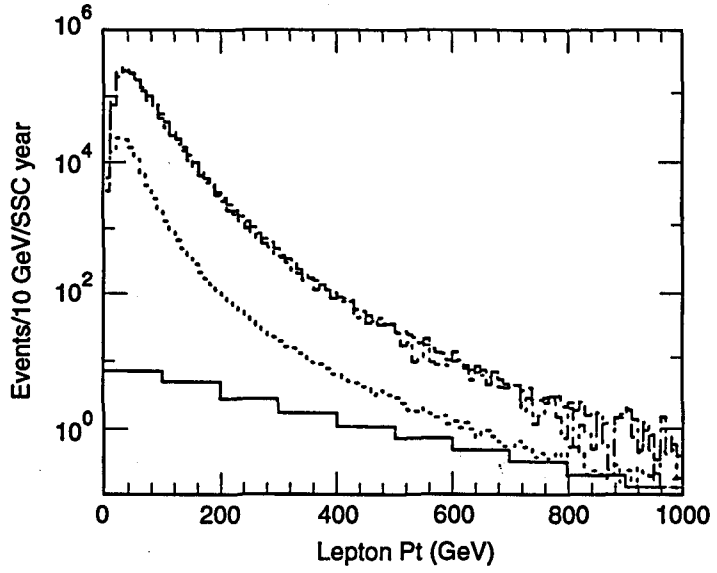


**Figure 51.** The lepton transverse momentum distribution expected for the $W^+W^+$ signal and backgrounds (there are two entries per event, one for each lepton). The signal is shown as the solid histogram, the dashed histogram is for $t\bar{t} \rightarrow W^+W^- + X$, and the dot-dashed histogram is for $t\bar{t} \rightarrow W^+b\bar{b} + X \rightarrow \ell^+\ell^+ + X$. Note that the curves for these two backgrounds sources lie on top of each other. The dotted histogram is for the direct production of opposite-sign $q\bar{q} \rightarrow W^+W^-$ background.

## Summary

The SDC design is capable of finding a standard model Higgs over the full mass range to even the highest masses. SUSY models are more difficult to disentangle, but some signals will likely be visible. (Evidence for SUSY itself is no problem.) The strong $WW$ scattering signal—difficult to extract even at SSC—appears possible albeit requiring a few years' running time. The theoretical uncertainty surrounding the nature of electroweak symmetry breaking implies that detection of a signal at, say, 200 GeV, decaying to $ZZ$ will not be enough to be sure of the physics. Full exploration of the complete mass range and as many decay modes as possible are necessary to strongly limit the available theoretical phase space. Studies performed thus far with realistic detector simulations show that the SSC can cover the full mass range necessary. Detector designs for LHC experiments should be available within a year to properly assess the limits to the capability of the proposed LHC machine.

## DETECTOR DESIGN IMPLICATIONS

The process of optimizing the SDC detector design to best match the physics goals of the collaboration requires identification of those physics processes that put the most stringent requirements on the detector performance. From the discussion above, one readily sees that detection of the Higgs sector, with its typical four-body decay modes, *requires* that the detector subsystems be designed to work together effectively.

Space does not permit a full discussion here of all the tradeoffs in the SDC design. A few comments concerning the impact of the physics goals on the calorimeter design are appropriate here. The angular coverage of the calorimeter is set by need to

retain high efficiency for the Higgs signal (lepton ID for $|\eta| < 3$), and by the need to have clean signals for gluino production ($|\eta| < 6$). The energy resolution and linearity requirements become mass resolution requirements for width determination or background suppression capability. Position resolution and particle identification capability are determined by the need to provide adequate segmentation to reduce backgrounds. Timing information must be accurate enough to tag the beam crossing in which the event occurred to simplify the trigger and DAQ system design. Tables 4–6 summarize the SDC calorimeter requirements.

Table 4. Performance Requirements on the SDC Calorimeter.

| Parameter | Requirement | Basis |
|---|---|---|
| $\eta$ max for $e^{\pm}$ ID | 2.5 | $H \rightarrow 4e, 2e2\mu$ |
| EM efficiency loss in $\|\eta\| < 2.5$ | $< 5\%$ | electron ID |
| $\eta$ max for jets | 5 | SUSY searches |
| gaps in full jet coverage, $\|\eta\| < 5$ | $\leq 1\%$ | Missing-$E_t$ |
| EM energy resolution | | $H \rightarrow \gamma\gamma, Z' \rightarrow ee$ |
| stochastic term | $\leq 15\%/\sqrt{E_t}$ | |
| constant term | $\leq 1\%$ | |
| EM transverse segmentation | 0.05 | $H \rightarrow 4e, H \rightarrow \gamma\gamma$ |
| Hadronic energy resolution | | dijet mass resolution |
| stochastic term | $\leq 70\%/\sqrt{E_t}$ | |
| constant term (single $\pi^{\pm}$) | $\leq 6\%$ | |
| Hadronic transverse segmentation | 0.10 | dijet mass resolution |
| EM residual nonlinearity | $\leq 1\%, E_t > 10$ GeV | $ee, \gamma\gamma$ mass resolution |
| Jet residual nonlinearity | $\leq 1\%/$ TeV$, E_t > 2$ TeV | compositeness search |
| Dynamic range (EM and HAC) | 20 MeV–4 TeV | $e$ ID, compositeness |
| EM depth | 22/25 $X_0$ | $ee, \gamma\gamma$ mass resolution |
| Calorimeter depth ($\eta = 0$) | $\geq 10\ \lambda$ | dijet mass resolution |

Table 5. Performance Requirements on the Shower Maximum Detector.

| Parameter | Requirement |
|---|---|
| Strip width | $< 1.5$ cm |
| Resolution $r - \phi$ and $z$ | $< 3$ mm |
| Resolution on relative energy (strip-strip) | $< 10\%$ |
| Strip length ($\Delta\eta$ or $\Delta\phi$) | $\leq 0.2$ |
| Cross talk | $\leq 0.5\%$ after correction |

Table 6. Performance Requirements on the Forward Calorimeter.

| Parameter | Requirement |
|---|---|
| Energy resolution | $< 10\%$ at 1 TeV |
| Transverse segmentation, $\eta = 3$ | 0.2 |
| $\eta = 5$ | 0.4 |
| Time resolution | $\sigma_t < 5$ ns, $E_t > 50$ GeV |
| Noise | $\sigma_{E_t} < 30$ GeV |
| $\eta$ coverage, jet axis | $3 \leq \lvert\eta\rvert \leq 5$ |
| (physical) | $2.8 \leq \lvert\eta\rvert \leq 6$ |

## CONCLUSIONS

The SSC is the tool of choice for future progress in particle physics. The SDC design is well advanced and appears capable of exploiting many of the physics opportunities made available by the SSC. We will see within a year designs for the SSC GEM experiment, as well as other high-$p_t$ experiments at LHC. Studies of those designs with detailed detector models will allow proper assessment of the capabilities and limitations of the SSC and LHC experimental programs. The proposed upgrade program at the FNAL Tevatron will provide experience relevant to the eventual SSC program, as the experimental community continues to push there the limits of understanding of standard model phenomenology in the high-rate, high-$p_t$ environment. However, the risk of discovery is much higher for any of a number of possible standard model extensions at the SSC. The ability of the proposed detector designs to cover a wide range of *expected* new physics gives confidence that the designs will be capable of discovering *unexpected* new phenomena hoped for at the SSC.

## ACKNOWLEDGEMENTS

The author thanks K. Einsweiler and M. Mangano for their valuable help in preparing these notes. Discussions with M. Chanowitz, G. Kane, and F. Paige helped clarify numerous points. Thanks also to my SDC collaborators, with whom I have had many useful discussions. Lastly, thanks to T. Ferbel, who did a fine job of organizing a very pleasant environment for the school.

## REFERENCES

1. J. Peoples *et al.*, Fermilab HEPAP subpanel presentations, 1992.
2. SSC Site-Specific Conceptual Design Report, July 1990.
3. SDC Technical Design Report, April 1992.
4. GEM Expression of Interest, July 1991.
5. W. Burgett *et al.*, "Full Power Test of a String of Magnets Comprising a Half-Cell of the Superconducting Super Collider," SSCL-Preprint-162, October 1992.
6. SSC-250, Dec. 1989.
7. CDF, PRD 45, 3921 (1992).
8. CDF, PRL 68, 1463 (1992).
9. CDF, PRL 68, 1104 (1992).
10. A. Beretvas, *Proc. of the 1990 Summer Study on High Energy Physics*, Snowmass (1990).
11. SDC Technical Design Report, April 1992.

12. For a review, see Eichten, Hincliffe, Lane, and Quigg (EHLQ), *Rev. Mod. Phys.* **56**, 579 (1984).
13. For a useful review of the kinematics, see the Appendix in Owens, *Rev. Mod. Phys.* **59**, 465 (1987).
14. Barger, Snowmass 1986, p. 224.
15. Berger and Chanowitz, *Phys. Lett.* **B263**, 509 (1991).